



ELSEVIER

Contents lists available at ScienceDirect

## International Journal of Plasticity

journal homepage: [www.elsevier.com/locate/ijplas](http://www.elsevier.com/locate/ijplas)

# Large-deformation crystal plasticity simulation of microstructure and microtexture evolution through adaptive remeshing

Karo Sedighiani<sup>a,\*,a,b</sup>, Vitesh Shah<sup>a</sup>, Konstantina Traka<sup>a,b</sup>, Martin Diehl<sup>a,c,d</sup>, Franz Roters<sup>a</sup>, Jilt Sietsma<sup>b</sup>, Dierk Raabe<sup>a</sup>

<sup>a</sup> Max-Planck-Institut für Eisenforschung, Max-Planck-Str. 1, Düsseldorf 40237, Germany

<sup>b</sup> Department of Materials Science and Engineering, Delft University of Technology, Mekelweg 2, CD Delft 2628, The Netherlands

<sup>c</sup> Department of Materials Engineering, KU Leuven, Kasteelpark Arenberg 44, Leuven 3001, Belgium

<sup>d</sup> Department of Computer Science, KU Leuven, Celestijnenlaan 200 A, Leuven 3001, Belgium

## ARTICLE INFO

## Keywords:

Crystal plasticity  
Large deformation  
Microstructure evolution  
Adaptive meshing  
Spectral method  
Finite element method

## ABSTRACT

The capability of high-resolution modeling of crystals subjected to large plastic strain is essential in predicting many important phenomena occurring in polycrystalline materials, such as microstructure, deformation localization and in-grain texture evolution. However, due to the heterogeneity of the plastic deformation in polycrystals, the simulation mesh gets distorted during the deformation. This mesh distortion deteriorates the accuracy of the results, and after reaching high local strain levels, it is no longer possible to continue the simulation. In this work, two different adaptive remeshing approaches are introduced for simulating large deformation of 3D polycrystals with high resolution under periodic boundary conditions. In the first approach, a new geometry with a new mesh is created, and then the simulation is restarted as a new simulation in which the initial state is set based on the last deformation state that had been reached. In the second approach, the mesh is smoothened by removing the distortion part of the deformation, and then the simulation is continued after finding a new equilibrium state for the smoothed mesh and geometry. The first method is highly efficient for conducting high-resolution large-deformation simulations. On the other hand, the second method's primary advantage is that it can overcome periodicity issues related to shear loading, and it can be used in conjunction with complex loading conditions. The merits of the methodologies are demonstrated using full-field simulations performed using a dislocation-density-based crystal plasticity model for Interstitial free (IF-) steel. Particular emphasis is put on studying the effect of resolution and adaptive meshing. The algorithms presented have been implemented into the free and open-source software package, DAMASK (Düsseldorf Advanced Material Simulation Kit).

## 1. Introduction

Metallic materials for structural applications are produced as polycrystals, i.e. they consist of many grains, each with a specific crystallographic orientation. As a result, the level of plastic deformation in a strained polycrystal varies from crystal to crystal, depending on its orientation, geometry, neighboring crystals, and loading conditions Choi (2003). In addition to such intergranular

\* Corresponding author.

E-mail address: [k.sedighiani@mpie.de](mailto:k.sedighiani@mpie.de) (K. Sedighiani).

<https://doi.org/10.1016/j.ijplas.2021.103078>

Received 13 May 2021; Received in revised form 23 July 2021; Accepted 2 August 2021

Available online 6 August 2021

0749-6419/© 2021 The Author(s). Published by Elsevier Ltd. This is an open access article under the CC BY license

(<http://creativecommons.org/licenses/by/4.0/>).

deformation heterogeneity, significant intragranular heterogeneity, i.e. localized continuous or discontinuous orientation spread within a grain forms during plastic deformation (Beaudoin et al., 1996; Cappola et al., 2021; Oddershede et al., 2015; Raabe et al., 2004; Sachtleber et al., 2002; Wang et al., 2018; Zhang et al., 2015).

The characterization of such localized deformations and microstructures formed during the deformation of polycrystalline materials is vital in developing a thorough physical understanding of the underlying mechanisms behind localization phenomena (Dao and Lit, 2001; Tasan et al., 2014b) such as fracture (Diehl et al., 2017c; Proudhon et al., 2016a), shear banding (Bate, 1999; Forest, 1998; Jia et al., 2012; Kanjarla et al., 2010; Kasemer and Dawson, 2020; Sarma and Dawson, 1996), and nucleation during recrystallization (Alaneme and Okotete, 2019; Chen et al., 2015; Diehl and Kühbach, 2020; Kim et al., 2017; Traka et al., 2021; Zhao et al., 2016). Crystal plasticity simulations (Roters et al., 2010) have been proven to be powerful tools for modeling and predicting the evolution of such deformation heterogeneities and the associated complex mechanical fields (Chen et al., 2019; Connolly et al., 2020; Dequiedt and Denoual, 2021; Diehl et al., 2017a; 2017b; 2019; Gierden et al., 2021; Jalili and Soltani, 2020; Khadyko et al., 2016; Liang et al., 2020; van Nuland et al., 2021; Reuber et al., 2014; Tasan et al., 2014a; Vidyasagar et al., 2018; Zhang et al., 2018). These models are developed based on physical mechanisms such as glide of dislocations on preferred slip systems and the interaction of dislocations with various defects (Roters et al., 2010).

The amount of detail that can be observed using a crystal plasticity simulation strongly depends on the simulation resolution (Diard et al., 2005; Lim et al., 2019; Ritz and Dawson, 2009; Zhao et al., 2007). A low-resolution simulation with only one or a few elements per crystal is sufficient to predict macro-scale (global) data such as global crystallographic texture (Sarma and Dawson, 1996) or stress-strain response (Diard et al., 2005). However, to achieve a more detailed description of meso-scale deformation localization effects, the simulation resolution needs to be increased significantly, even to hundreds of thousands of elements per crystal (Diard et al., 2005; Lim et al., 2019; Ritz and Dawson, 2009; Zhao et al., 2007).

At the same time, many of these localization phenomena emerge at medium to large strains (Kweon and Raja, 2017; Savage et al., 2020). For example, microstructures in pure nickel evolve from typical dense dislocation walls and microbands to lamellar boundaries in a strain range of 0.8 to 2.7 (Hughes and Hansen, 2000). Therefore, the capability to perform high-resolution large-deformation simulations provides an indispensable means for predicting strain localization and analyzing microstructure evolution.

Typically, continuum mechanical problems involving the deformation of solid materials are formulated in a Lagrangian context, i.e. the mesh is attached to the deformable body and deforms with a change in the shape of the material. However, the relative position of the material points and the mesh (nodes) remains fixed. This means that the mesh gets distorted due to the strain localization. The mesh distortion initially introduces errors in the solution and delays convergence. Ultimately, the distortion becomes too large, and the simulation fails to converge. The maximum possible applied strain depends on many factors, such as the constitutive law, loading conditions, polycrystal morphology, and the simulation resolution (Lim et al., 2019). A higher simulation resolution allows capturing more detailed localized deformation features, which results in earlier mesh convergence issues.

In order to overcome the mesh distortion problem and reach larger strains, it is required to remove the mesh distortion and reconstruct a new undistorted mesh—a process that is called remeshing (Frydrych et al., 2019; Kim et al., 2015; Prakash et al., 2015; Proudhon et al., 2016; Quey et al., 2011; Resk et al., 2009). After building the new mesh, the simulation can be restarted on the reconstructed mesh. The most challenging step in any remeshing algorithm is transferring the state variables from the distorted mesh to the newly reconstructed mesh. The hurdle is that reaching an exact identity between the deformed and the remeshed stage is impossible, and some information is always lost. However, the two stages must be sufficiently similar so that the two configurations reproduce almost identical responses.

In general, two different approaches are used for mapping the state variables between the two stages. According to the first mapping approach, the value of the state variables at each point in the newly generated undistorted mesh is determined directly from the closest corresponding point of the deformed mesh (Kim et al., 2015; Resk et al., 2009). The second mapping approach uses the interpolation of the state variables at adjacent elements to determine the values of the state variables at the new undistorted elements (Frydrych et al., 2019).

The interpolation of state variables is problematic in large strain crystal plasticity formulations. This is because some state variables, such as the crystallographic orientations, are not spatially continuous. In addition, there is no monotonic relation between mechanical behavior and orientation, i.e. interpolating between two crystals with the same behavior, but different orientations might result in an orientation with different behavior. This also holds if crystal symmetries are taken into account. Furthermore, the interpolation of some tensorial quantities is not straightforward. For example, interpolation of the deformation gradient tensor  $\mathbf{F}$  might result in a non-compatible displacement field.

Prakash et al. (2015) used a spherical linear interpolation developed by Shoemaker (1985) to interpolate the crystallographic orientations and the rotation tensor. They applied this approach to a mean-field visco-plastic self-consistent model. Kim et al. (2015) compared the nearest neighbor mapping-based approach with an interpolation-based approach for full-field crystal plasticity simulations. They found that the nearest neighbor mapping-based method performs better than the interpolation-based approach. Frydrych et al. (2019) developed two different interpolation-based methods that consider the spherical space of orientations. They performed a comprehensive comparison between these two methods and an approach based on the nearest neighbor mapping. Although they observed that all three methods provide almost identical macroscopic mechanical responses, they concluded that the nearest neighbor mapping-based approach predicts less reliable results for some state variables than the two interpolation-based methods. This is contrary to what Kim et al. (2015) observed. It should be noted that Frydrych et al. (2019) studied only low-resolution polycrystal examples with idealized grain geometry, which might be the reason for the interpolation-based methods' better performance.

Although the interpolation approach may reduce the jumps and provide a more continuous map of the state variables, this comes at the cost of smoothing away physically meaningful sharp localized deformation features. Therefore, the interpolation approach is less

suited when aiming at the simulation of strain localization and in-grain orientation spread. This may not be a problem for low-resolution simulations, in which the main outputs are macroscopic crystallographic texture or stress-strain curve. However, this impacts the output of high-resolution simulations, where capturing deformation localization and microstructure evolution is the primary objective.

This paper introduces two remeshing techniques to overcome the mesh distortion problem in high-resolution crystal plasticity simulations. Both approaches use a nearest-neighbor mapping algorithm to transfer the state variables from the distorted mesh to a new undistorted mesh. This study focuses specifically on designing remeshing methodologies that are efficient and applicable for high-resolution 3D crystal plasticity simulations of representative volume elements (RVEs) under periodic boundary conditions. With this in mind, a global adaptive scheme is implemented in both approaches, allowing the free adjustment of the number of elements in the three coordinate directions at each remeshing step. The adaptivity scheme provides a tool to increase the resolution based on the problem and the deformation heterogeneity to efficiently and adequately model the microstructure evolution. In this work, a Fast Fourier Transform (FFT) based spectral method is used to solve the partial differential equations for static equilibrium. Accordingly, the elements (voxels) used in the simulations are rectangular cuboids, i.e. right-angled hexahedrons. These elements are conceptually similar to reduced-integration, linear brick elements used in finite element analysis, i.e. cuboid elements with just a single integration point located at the element's centroid.

This paper thoroughly examines and elaborates on the remeshing methodologies' capability in predicting the deformation heterogeneity and microstructure evolution at large strains. For this purpose, the crystal plasticity framework and the basic formulations is first explained in Section 2. Then, in Section 3, the two remeshing approaches are explained in detail. In Section 4, various high-resolution examples are used to examine and validate the methodologies by answering the following questions: How accurate are the two introduced methodologies (Section 4.1)? What is the effect of adaptivity on the accuracy and simulation outputs (Section 4.2)? What are the advantages and disadvantages of the two remeshing approaches (Section 4.3)? How to overcome challenges related to remeshing for problems involving shear loading (Section 4.4)? How does simplifying a 3D simulation to a quasi-3D simulation affect the results (Section 4.5)? Finally, the methodologies are used to predict the deformation behavior and microstructure evolution during the large deformation of a 3D polycrystal with high resolution (Section 4.6).

## 2. Crystal plasticity framework

We use DAMASK (Roters et al., 2019) to conduct the crystal plasticity simulation together with a spectral solver. This solver uses Fast Fourier Transforms to find an approximate solution for the system of governing Partial Differential Equations (PDEs) and boundary conditions (Eisenlohr et al., 2013; Shanthraj et al., 2015). The following section provides a brief summary of the basic formulations, for more detail on the spectral solver implemented in DAMASK see (Eisenlohr et al., 2013; Roters et al., 2019; Shanthraj et al., 2015).

### 2.1. Multiplicative decomposition

The kinematics in DAMASK for elasto-plastic behavior is defined within the finite deformation framework. According to this framework, the deformation gradient tensor is written as the product of two tensors:

$$\mathbf{F} = \mathbf{F}_e \mathbf{F}_p, \quad (1)$$

where  $\mathbf{F}_p$  is the plastic deformation gradient, and  $\mathbf{F}_e$  is the elastic deformation gradient. The main reasoning for such decomposition is to distinguish between elastic deformation, a reversible deformation resulting from stretching of atomic bonds, and plastic deformation, an irreversible lattice-preserving deformation resulting from, for instance, dislocation slip.

The decomposition order in Eq. 1 allows considering the anisotropy and dependency of a constitutive law on crystallographic orientation. For a polycrystal analysis, stiffness tensors, slip plane normals, and slip directions of each crystal must be specified in a global coordinate system. Such tensorial quantities are typically defined in the lattice coordinate system to avoid unnecessary rotations of tensorial quantities. For this purpose, following Ma et al. (2006), the initial value of  $\mathbf{F}_p$  is set as the initial crystal orientation  $\mathbf{O}_0$ :

$$\mathbf{F}_p(t=0) = \mathbf{O}_0. \quad (2)$$

Therefore, the initial reference configuration for all crystals is the cube orientation. Then,  $\mathbf{F}_e^0 = \mathbf{F}_e(t=0)$  is set as  $\mathbf{O}_0^T$  to achieve the desired identity tensor,  $\mathbf{I}$ , for the initial deformation gradient tensor:

$$\mathbf{F}^0 = \mathbf{F}_e^0 \mathbf{F}_p^0 = \mathbf{I}. \quad (3)$$

The current crystal orientation  $\mathbf{O}$  can then be calculated by polar decomposition of the current elastic deformation:

$$\mathbf{F}_e = \mathbf{V}_e \mathbf{O}^T, \quad (4)$$

where  $\mathbf{V}_e$  is the elastic left stretch tensor.

## 2.2. Flow kinematics

The evolution of the plastic deformation gradients is calculated as:

$$\dot{\mathbf{F}}_p = \mathbf{L}_p \mathbf{F}_p, \quad (5)$$

where  $\mathbf{L}_p$  is the velocity gradient.  $\mathbf{L}_p$  is calculated from stress, here the second Piola-Kirchhoff stress  $\mathbf{S}$ , and it depends on the underlying microstructure through the plasticity constitutive law:

$$\mathbf{L}_p = f(\mathbf{S}, \dots). \quad (6)$$

Assuming a Hookean elastic constitutive law, the second Piola-Kirchhoff stress is given as

$$\mathbf{S} = \mathbb{C} : \mathbf{E}, \quad (7)$$

where  $\mathbf{E}$  is the Green-Lagrange strain tensor:

$$\mathbf{E} = \frac{1}{2} (\mathbf{F}_c^T \mathbf{F}_c - \mathbf{I}). \quad (8)$$

## 2.3. Inelastic flow relations

The plastic deformation in crystalline materials occurs on well-defined slip systems specific to a crystallographic lattice. The plastic velocity gradient  $\mathbf{L}_p$  is thus composed of the superposition of all the individual resolved plastic shear rates on these systems  $\alpha$ :

$$\mathbf{L}_p = \sum_{\alpha} \dot{\gamma}^{\alpha} (\mathbf{s}_s^{\alpha} \otimes \mathbf{n}_s^{\alpha}), \quad (9)$$

where  $\mathbf{s}_s^{\alpha}$  and  $\mathbf{n}_s^{\alpha}$  are respectively the unit vectors along the shear direction and shear plane normal.

## 2.4. Constitutive model

In DAMASK (Roters et al., 2019), a variety of constitutive laws are available, and they can be used for different crystal structures and definitions of slip system families such as face-centered cubic (fcc), body-centered cubic (bcc), hexagonal (hex), and body-centered tetragonal (bct) lattice types. These constitutive laws rely on state variables that constitute and track the deformation history, e.g. the critical resolved shear stress for the case of the phenomenological constitutive law or the dislocation density for the case of the dislocation-density-based constitutive law. For the case studies presented in this paper, the simulations are conducted using the dislocation-density-based constitutive law as outlined in (Ma and Roters, 2004; Sedighiani et al., 2021). However, the remeshing approaches, introduced in Section 3, are independent of the constitutive law and they can be used with any crystal plasticity model. The material parameters are chosen to be according to those identified for Interstitial Free (IF) steel by (Sedighiani et al., 2020, 2021).

## 3. Methodology

### 3.1. Remeshing techniques

This section explains two remeshing techniques developed in this work to overcome the mesh distortion problem. Besides, the differences between the approaches are elaborated.

#### 3.1.1. Mesh replacement method

The mesh replacement method is based on replacing the distorted mesh with a newly created undistorted mesh. According to this remeshing technique, a new (cuboid) geometry is first created, which matches the average outer dimensions of the deformed geometry considering the periodicity of the configuration. Then, the original mesh is replaced by a new mesh assigned to this new geometry. Finally, the simulation is restarted using the new configuration as a new simulation without any mesh distortion. This is physically equivalent to replacing the deformation gradient tensor with the identity tensor and the full relaxation of the elastic deformation; see Section 3.2.1 for more information. The selection of the resolution for the new mesh is following an adaptive scheme, which allows updating the resolution during the deformation at each remeshing step. The adaptivity is described and studied in more detail in Section 3.3.

Once the new geometry and the new mesh are available, the state variables from the deformed stage are mapped onto the newly created mesh. The mapping is performed using a nearest-neighbor mapping algorithm to transfer the state variables from the deformed state to the points in the new mesh. The transferred state variables and the mapping procedure are discussed in more detail in Section 3.2.

The similitude between the deformed configuration and the remeshed configuration for the mesh replacement method is tested using the two examples shown in Fig. 1(a-b). Fig. 1(a) illustrates a high-resolution quasi-3D, i.e. one element in the transverse

direction, bicrystal RVE with a mesh of  $60 \times 60$  elements. This example is selected because its deformation is heterogeneous, and, at the same time, its deformation results in a non-random distribution of the state variables, e.g. a bimodal distribution of the Euler angles. As a result, it is straightforward to trace any changes and evaluate the accuracy of the remeshing approach. The deformed configuration before and after remeshing is shown in Fig. 2 for this example. It is clear that most of the main features are captured and transferred to the remeshed RVE. The Kolmogorov-Smirnov test (Massey, 1951) is used to assess the accuracy of the remeshing and the similitude between the two stages. The Kolmogorov-Smirnov test quantifies the maximum difference between the cumulative distribution function of two distributions. The Kolmogorov-Smirnov values for both the total dislocation density and the rotation angle are 0.007. It is clear that such difference between the two cumulative distributions is negligible.

The rotation angle,  $|\Delta\theta|$ , is the absolute amount of rotation (re-orientation) a simulation point undergoes during the entire deformation history. It is calculated as:

$$|\Delta\theta| = \arccos\left\{\left[\frac{\text{tr}(\mathbf{O}\mathbf{O}_0^T) - 1}{2}\right]\right\}, \quad (10)$$

where  $\mathbf{O}$  and  $\mathbf{O}_0$  are the current and the initial orientation matrixes. The symbol  $\text{tr}()$  stands for the trace of a matrix.

The second example to study the accuracy of the mesh replacement method is a 3D polycrystal RVE, as shown in Fig. 1(b). The deformed configuration before remeshing and the remeshed configuration are shown in Fig. 2. Unlike the first example, the state variables' distribution for this example is close to a normal distribution. The Kolmogorov-Smirnov values for the total dislocation density and the rotation angle are 0.003 and 0.002, respectively. Again, the difference between the two cumulative distributions is negligible.

### 3.1.2. Mesh distortion control method

In the case of FFT-based spectral solvers, which always operate on a cubic domain that is infinitely repeated, the mesh replacement method can be used only with loading conditions that preserve the periodicity of the configuration, e.g. tensile, compression, or biaxial loading conditions. For this reason, this approach cannot be employed to simulate cases where the RVE is under loading conditions that involve a shear deformation. However, shear deformation is present in many industrial applications, and it is essential to be able to include such type of loading condition during large deformation of polycrystals. Therefore, a second approach, the mesh distortion control method, is developed to enable remeshing under shear loading. In Section 4.4, information about shear loading and the related challenges is given.

The mesh distortion control method is working based on smoothing the distorted mesh to continue the simulation in its current state. The new undistorted mesh is achieved by modifying the deformation map and removing the locally fluctuating part of the deformation, see Section 3.2.1. Since the average deformation is maintained, this remeshing technique can be used along with periodic configurations subjected to an arbitrary loading condition, such as those loading conditions involving a shear deformation, see Section 4.4 for more detail. This remeshing procedure also allows using the adaptivity scheme introduced in Section 3.3 for updating the simulation resolution at each remeshing step. Once the new undistorted mesh is available, the state variables from deformed stage are mapped onto the undistorted mesh. The mapping is performed using a nearest-neighbor mapping algorithm to transfer the state variables from the deformed state to the points in the smoothed mesh, i.e. the deformed state but without fluctuations. The transferred state variables and the mapping procedure are discussed in more detail in Section 3.2.

The similitude between the deformed and the remeshed configurations for the mesh distortion control method is tested using two examples, as shown in Fig. 1(c-d). Fig. 1(c) represents a quasi-3D bicrystal RVE similar to the one used in the previous section. However, here the orientations of the two grains are exchanged. The deformed bicrystal RVE before remeshing and after remeshing for this RVE is shown in Fig. 3. Obviously, the main features are captured and transferred to the remeshed configuration. The Kolmogorov-Smirnov values for the total dislocation density and the rotation angle distributions are 0.005 and 0.003, respectively. It is evident that the difference between the two distributions is negligible.

The second example to study the accuracy of the mesh distortion control method is a 3D polycrystal RVE, as presented in Fig. 1(d). The deformed and the remeshed configurations are shown in Fig. 3. The Kolmogorov-Smirnov values for the total dislocation density and the rotation angle are 0.001 and 0.003, respectively. Again, the difference between the two distributions is negligible.

## 3.2. Mapping variables

Mapping the microstructural and mechanical variables from the deformed state onto the new mesh is performed using a nearest-neighbor mapping algorithm that identifies the nearest point<sup>1</sup> in the original deformed mesh for each point in the newly created mesh (Maneewongvatana and Mount, 2001). The nearest neighbor is determined using the Euclidean distances measured between points in the deformed and the remeshed configurations. It should be noted that more than one point in the remeshed state might acquire their state variables from the same point during mapping. This is especially the case when the number of elements is increased using the adaptive meshing scheme introduced in Section 3.3. After assigning a corresponding point in the old configuration to each point in the new configuration, the microstructural and mechanical variables are transferred to the new configuration. Different processes are used here for different variables. In general, the variables are handled in three different ways, as explained in the following.

<sup>1</sup> Fourier points in the case of a spectral solver and integration points in the case of a finite element solver.

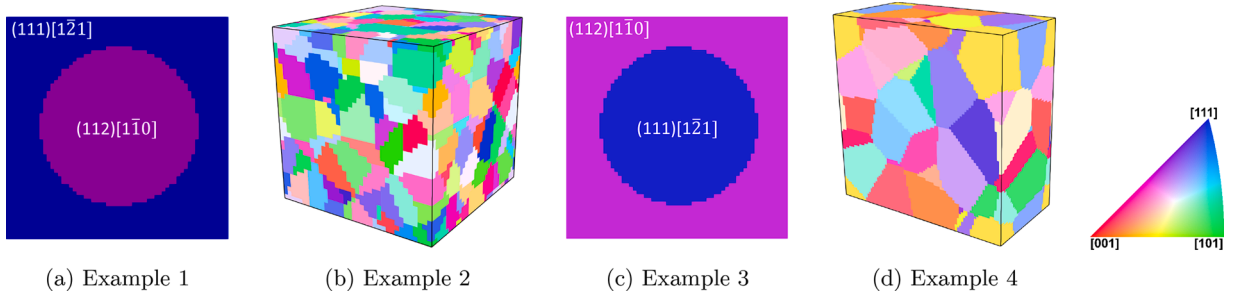


**Fig. 1.** Voxel representation of the RVEs used in the crystal plasticity simulations to show the capabilities of the remeshing approaches. The coloring follows the IPF color map parallel to the vertical direction. (a) Example 1: a quasi-3D RVE made of 2 grains with an initial mesh of  $60 \times 60$  elements. (b) Example 2: a 3D polycrystal RVE made of 216 grains with an initial mesh of  $36 \times 36 \times 36$  elements. (c) Example 3: a quasi-3D RVE made of 2 grains with an initial mesh of  $60 \times 60$  elements. (d) Example 4: a 3D polycrystal RVE made of 32 grains with an initial mesh of  $80 \times 40 \times 80$  elements.

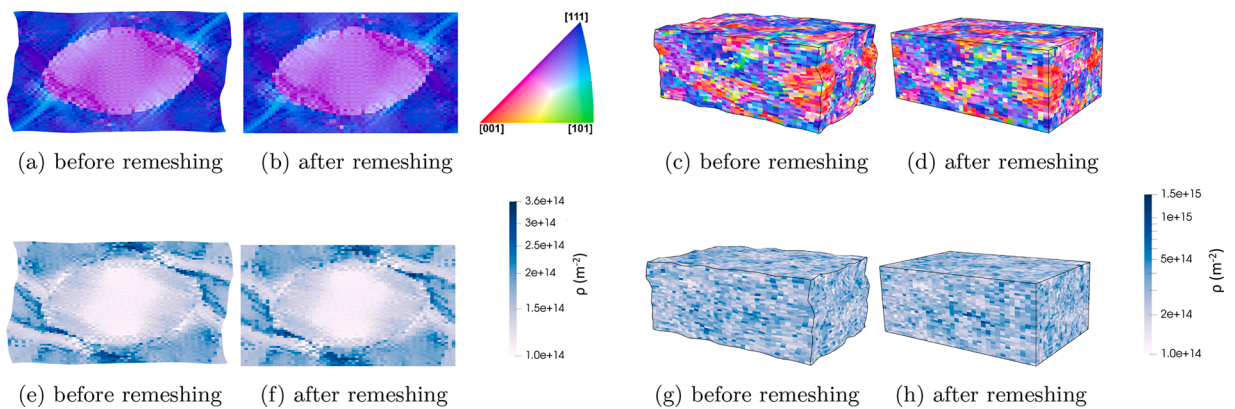


**Fig. 2.** The data mapping step for the mesh replacement method is examined by comparing the outputs before and after remeshing for Examples 1 and 2 presented in Fig. 1. (a-d) IPF color maps parallel to the loading (vertical) direction; (e-h) mobile dislocation density maps.

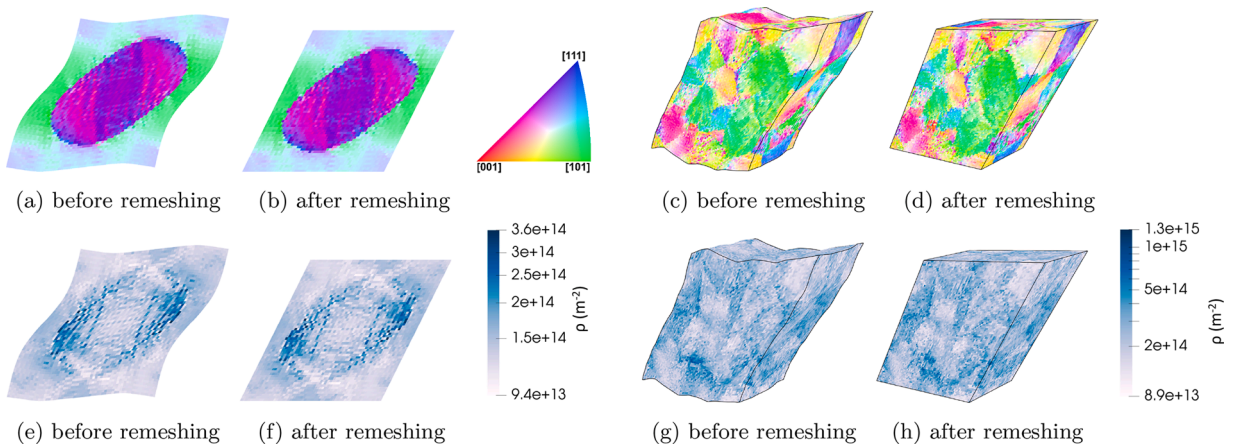


**Fig. 3.** The data mapping step for the mesh distortion control method is examined by comparing the outputs before and after remeshing for Examples 3 and 4 presented in Fig. 1. (a-d) IPF color maps parallel to the vertical direction; (e-h) mobile dislocation density maps.

### 3.2.1. Deformation gradient tensor

*Mesh replacement method.* The deformation gradient tensor is handled differently for the two remeshing methods. For the mesh replacement method, the deformation gradient tensor is replaced by the identity tensor, and the elastic deformation during the

remeshing procedure is fully relaxed. Since the elastic strains during large deformation are usually significantly smaller than the plastic strains, approximately two orders of magnitude, the relaxation of the elastic deformation has a negligible effect on the resulting mechanical fields at large plastic strains (Quey et al., 2011). Because of the full relaxation of the elastic deformation, the new configuration is in mechanical equilibrium.

*Mesh distortion control method.* In the mesh distortion method, the locally fluctuating part of the deformation map is calculated for each element, and then it is removed from the deformation. In other words, only the spatially homogeneous part of the deformation is maintained, i.e. the average deformation gradient tensor, which is also equal to the deformation gradient applied as a boundary condition. For this purpose, the deformation gradient tensor,  $\mathbf{F}$ , is split into the sum of a spatially homogeneous part,  $\bar{\mathbf{F}}$ , and a locally fluctuating part  $\tilde{\mathbf{F}}$ :

$$\mathbf{F} = \bar{\mathbf{F}} + \tilde{\mathbf{F}}. \quad (11)$$

Now the new undistorted mesh is generated using the modified deformation map,  $\chi^f(\mathbf{x})$ , as:

$$\chi^f(\mathbf{x}) = \chi(\mathbf{x}) - \tilde{\mathbf{F}}\mathbf{x} = \bar{\mathbf{F}}\mathbf{x}. \quad (12)$$

Here, a new mechanical equilibrium state for the undistorted mesh needs to be calculated, i.e. a state where zero net forces are acting on the material volume. Mathematically, for static equilibrium, this is expressed as (Roters et al., 2019):

$$\text{Div } \mathbf{P} = 0 \quad \text{in } \mathcal{B}_0. \quad (13)$$

### 3.2.2. Crystal orientations

As mentioned in Section 2.1, the initial crystal orientation of each simulation point is introduced via  $\mathbf{F}_p^0$ , and the initial  $\mathbf{F}_c^0$  is set as the inverse of  $\mathbf{F}_p^0$  to achieve the desired identity deformation gradient tensor at the beginning of the simulation. During the deformation, the orientation of the simulation points evolves according to the loading, orientation, and neighboring points. The current orientation of each simulation point can be calculated using the rotational part of the elastic deformation gradient tensor; see Eq. 4. With this in mind, during the remeshing step, the deformation gradient tensor is modified and updated to achieve an undistorted mesh. This adjustment in the deformation gradient tensor must be reflected in the plastic deformation tensor to achieve a correct initial state for the simulation points' current orientation. Since the mesh distortion is handled differently for the two remeshing methods, the plastic deformation gradient tensor must also be adjusted accordingly.

### 3.2.3. Mesh replacement method

In the mesh replacement method, the restart of the remeshing analysis is handled similar to a new simulation in which the initial state variables are modified according to the latest state of the deformation before remeshing. Moreover, according to this approach, the deformation gradient tensor is fully relaxed to the identity tensor. Therefore, to accommodate the current orientation of the crystal points, the plastic deformation tensor is replaced with current orientation of the simulation points, i.e.  $\mathbf{F}_p^r = \mathbf{O}$ . At the same time, the elastic deformation gradient tensor is set to the inverse of  $\mathbf{F}_p^r$ . The superscript "r" stands for the initial condition of the remeshed configuration before restarting the simulation.

### 3.2.4. Mesh distortion control method

According to the mesh distortion control method, the fluctuating part of the deformation is removed to overcome the distortion problem, and the deformation gradient tensor is adjusted to the average gradient deformation tensor. The deformation gradient tensor before restarting the simulation, i.e. after the remeshing step, can be written as:

$$\mathbf{F}^r = \bar{\mathbf{F}} = \mathbf{F}_c^r \mathbf{F}_p^r = \mathbf{F}_c \mathbf{F}_p^r. \quad (14)$$

Since the plastic deformation is much larger than the elastic deformation, it is assumed here that the fluctuating part belongs fully to the plastic deformation, and therefore  $\mathbf{F}_c^r = \mathbf{F}_c$ . The adjusted remeshed plastic deformation tensor,  $\mathbf{F}_p^r$ , can now be calculated as:

$$\mathbf{F}_p^r = \mathbf{F}_c^{-1} \bar{\mathbf{F}} = (\mathbf{F}_p \mathbf{F}^{-1}) \bar{\mathbf{F}}. \quad (15)$$

This newly calculated plastic deformation tensor includes the current orientation and the average plastic strain.

### 3.2.5. All other state variables

All other state variables, such as dislocation density or accumulated shear strain on each slip system, are directly mapped from the old simulation to the new simulation. This procedure follows an adaptable framework, and it allows mapping different state variables based on the constitutive law in use. As a result, the remeshing methodologies are flexible to be used with any crystal plasticity model.

### 3.3. An adaptive scheme for updating resolution

During large deformation, the elements' aspect ratio, i.e. the ratio of the element size in the stretching direction to the element size in the compression direction, can become very large. Extensively elongated elements introduce errors in the simulation and, more importantly, can prevent strain localization. To overcome this problem, we have implemented a global adaptive scheme for both remeshing approaches. This adaptive scheme is flexible and allows selecting any desired number of elements in the three coordinate directions independently at any remeshing step. Such ability to adapt the resolution according to the problem is crucial for large deformation simulations.

Fig. 4 (a) shows the IPF color map parallel to the loading direction for the deformed configuration. The remeshed configurations achieved using three different resolutions are shown in Fig. 4(b-d). Here, the remeshing is performed using the mesh replacement method, and the initial microstructure is according to the bicrystal example shown in Fig. 1(a). Fig. 5 shows the total dislocation density and the rotation angle distributions for these cases. It is clear from both figures that all the remeshing resolution cases selected here properly represent the deformed state. Although some improvement in the remeshing state can be observed for higher mesh resolutions, this improvement is subtle according to the Kolmogorov-Smirnov values presented in Table 1. The effect of remeshing resolution and adaptivity on the microstructure evolution is discussed in 4.2.

## 4. Results and discussion

### 4.1. Remeshing accuracy

In this study, two different remeshing approaches were introduced to solve the mesh distortion problem. It was shown that the deformed and the remeshed configurations are almost equivalent, and the mapping procedure can transfer the state variables accurately. Now the question arises, how does the remeshing procedure affect the microstructure and the mechanical fields developed during the simulation? To answer this question, we deform the RVEs to the largest achievable strain without remeshing. This simulated state is used as the reference state, and it is compared to the results obtained using different remeshing strategies. This comparison is used to analyze and discuss the accuracy of the remeshing approaches.

#### 4.1.1. Mesh replacement method

For the mesh replacement method, the bicrystal example presented in Fig. 1(a) is used for evaluating the remeshing approach. This RVE is subjected to a plane-strain compression up to 25% thickness reduction using different remeshing strategies:

- 1 step of 25% without remeshing (strategy A)
- 5 steps of 5% (strategy B)
- 3 steps of 10% + 10% + 5% (strategy C)
- 2 steps of 15% + 10% (strategy D)

Strategy A, the case without remeshing, is used as a reference case to evaluate the accuracy of the remeshing method. The stress-strain curves obtained using different remeshing strategies are compared to the reference case in Fig. 6. After a very small recovery strain, the remeshed configuration reaches the same stress level as the case without remeshing, and the effect of the remeshing process on the stress-strain curves becomes negligible. Generally, for the minimal impact of the remeshing on the results, the remeshing strain should be selected large enough relative to this recovery strain.

The IPF color map parallel to the loading (vertical) direction, the mobile dislocation density maps, and orientation distribution functions (ODFs) for the different remeshing strategies are shown in Fig. 7. Fig. 8 illustrates the distributions of the total dislocation density and the rotation angle for the different remeshing strategies. There is a very good agreement between results obtained using remeshing strategies C and D with reference case A. However, a comparison between results obtained using remeshing strategy B and reference case A reveals some small differences in the predicted shape of the central grain. The stress-strain curve for strategy B also shows a little deviation from the reference case. The fluctuation part of deformation, which is directly related to the deformation localization, is not fully developed at small strains. Therefore, when small remeshing strains are used, the localized deformation may

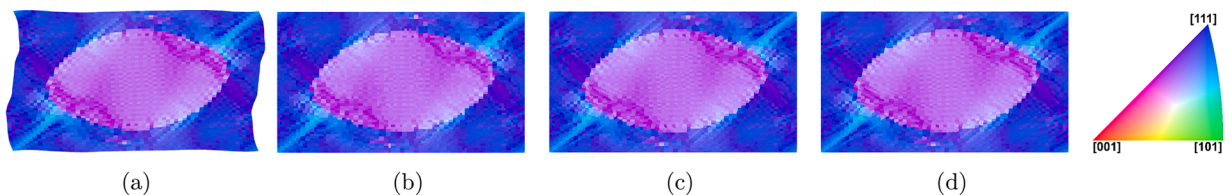


Fig. 4. Effect of remeshing resolution on the similitude of the configurations before and after remeshing. The figures show the IPF color map parallel to the loading (vertical) direction for the example presented in Fig. 1(a) subjected to 25% thickness reduction: (a) before remeshing with initial mesh of  $60 \times 60$  elements, (b) remeshed to a new mesh of  $107 \times 60$  elements, (c) remeshed to a new mesh of  $214 \times 120$  elements, (d) remeshed to a new mesh of  $428 \times 240$  elements.

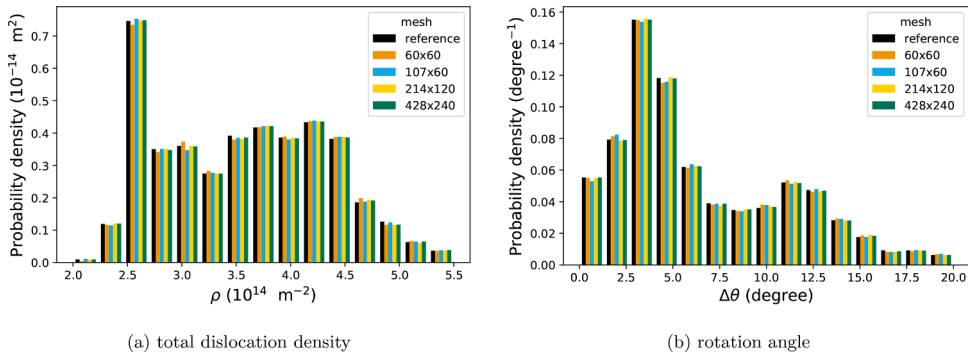


Fig. 5. Influence of the remeshing resolution on the distribution of (a) total dislocation density, (b) rotation angle. The initial number of elements for the reference configuration is  $60 \times 60$ . The results are shown for the cases presented in Fig. 4.

Table 1  
The Kolmogorov-Smirnov values obtained for cases remeshed with different resolutions.

Resolution		$60 \times 60$	$107 \times 60$	$214 \times 120$	$428 \times 240$
Kolmogorov-Smirnov value	$\rho^a$	0.007	0.005	0.004	0.002
	$ \Delta\theta $	0.007	0.005	0.003	0.001

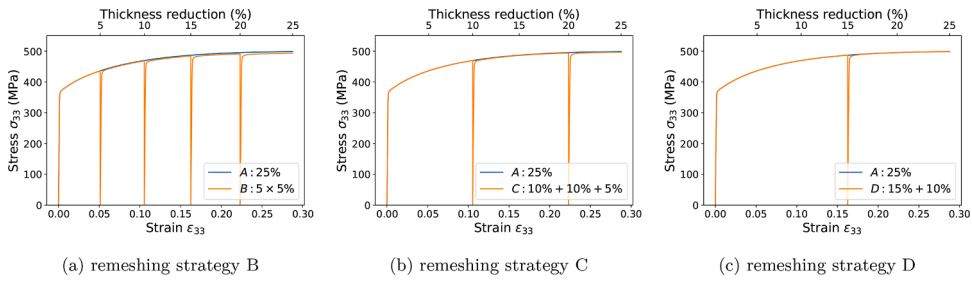


Fig. 6. Influence of the remeshing strategy on the stress-strain curves. The y-axis and x-axis show respectively the stress and the logarithmic strain in the compression direction. The blue curve shows the stress-strain curve for reference case A.

not be fully captured during the remeshing process. As a result, frequent remeshing after a small strain attenuates strain localization. However, when the remeshing procedure is applied in larger strain steps, i.e. remeshing strategies C and D, the deviation between the remeshed simulations and the reference simulation becomes small and negligible. The Kolmogorov-Smirnov values for all cases are listed in Table 2.

Although early remeshing can smoothen the localized deformation and affect the outputs' accuracy, remeshing after a large strain, late remeshing, can also deteriorate the accuracy and the computational efficiency. Large distortion in the mesh introduces numerical errors in the simulation. Therefore, as the first drawback, when the remeshing procedure is applied late after the distortions become too large, the state variables will include errors. These numerical errors would be transferred during the remeshing process. The mesh distortion and numerical errors also can affect the simulations' convergence and computational cost. We observed that the number of iterations needed for reaching convergence is directly related to the level of mesh distortion.

4.1.2. Mesh distortion control method

For the mesh distortion control method, the bicrystal example presented in Fig. 1(c) is used for evaluating the remeshing approach. The RVE is subjected to a simple shear of 0.5 using different remeshing strategies:

- 1 step of 0.5 without remeshing (strategy E)
- 3 steps of 0.2 + 0.2 + 0.1 (strategy F)
- 2 steps of 0.25 + 0.25 (strategy G)
- 2 steps of 0.4 + 0.1 (strategy H)

Strategy E, the case without remeshing, is used as a reference case to evaluate the accuracy of the remeshing method. The stress-strain curves obtained using different remeshing strategies are compared to the reference case in Fig. 9. The recovery strain for the

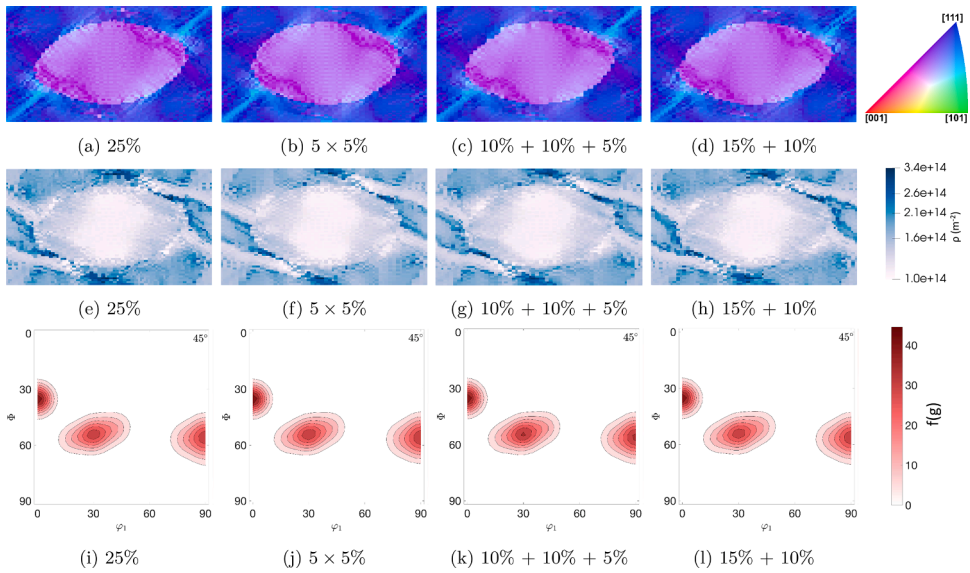


Fig. 7. Influence of the remeshing strategy on the simulation outputs. (a-d) IPF color maps parallel to the loading (vertical) direction, (e-h) mobile dislocation density maps, and (i-l) orientation density f(g) maps obtained from the ODFs. The results are for the example presented in Fig. 1(a).

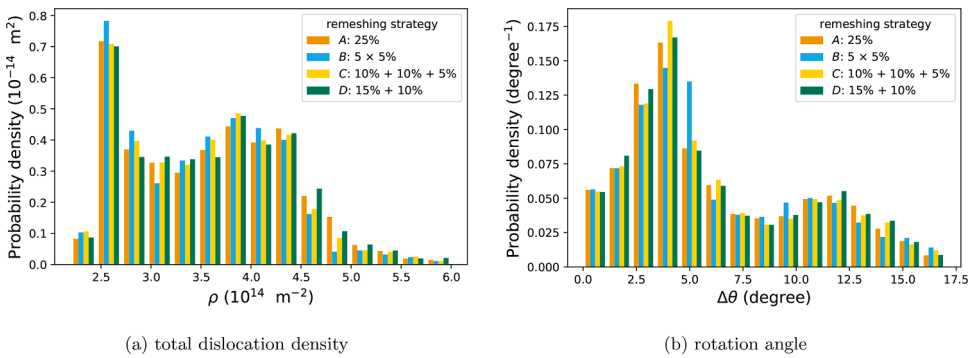


Fig. 8. Influence of the remeshing strategy on the distribution of (a) total dislocation density, (b) rotation angle. strategy A show the outputs for the case without remeshing.

Table 2

The Kolmogorov-Smirnov values obtained from different remeshing strategies.

strategy	mesh replacement method			mesh distortion control method		
	5 × 5%	10% + 10% + 5%	15% + 10%	0.2 + 0.2 + 0.1	0.25 + 0.25	0.4 + 0.1
$\rho^a$	0.072	0.046	0.017	0.025	0.022	0.019
$ \Delta\theta $	0.038	0.029	0.025	0.028	0.036	0.028

mesh distortion control method is much smaller than for the mesh replacement method, and the remeshed configuration immediately reaches the same stress level as the case without remeshing.

The IPF color map parallel to the vertical direction, the mobile dislocation density maps, and orientation distribution functions (ODFs) for the different remeshing strategies are shown in Fig. 10. Fig. 11 illustrates the distributions of the total dislocation density and the rotation angle for different remeshing strategies. There is a very good agreement between results obtained using different remeshing strategies and the reference case E. The Kolmogorov-Smirnov values for all the remeshing strategies are listed in Table 2.

#### 4.2. Adaptivity and mesh refinement effects

The global adaptive scheme implemented in both remeshing approaches allows adjusting the number of elements in the three

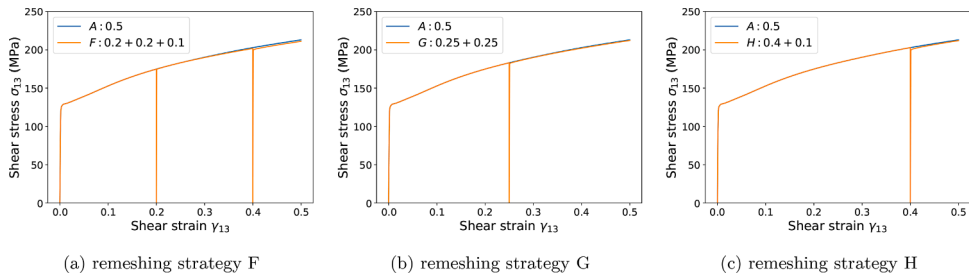


Fig. 9. Influence of the remeshing strategy on the stress-strain curves. The y-axis and x-axis show respectively the stress and the logarithmic strain in the compression direction. The blue curve shows the stress-strain curve for reference case E.

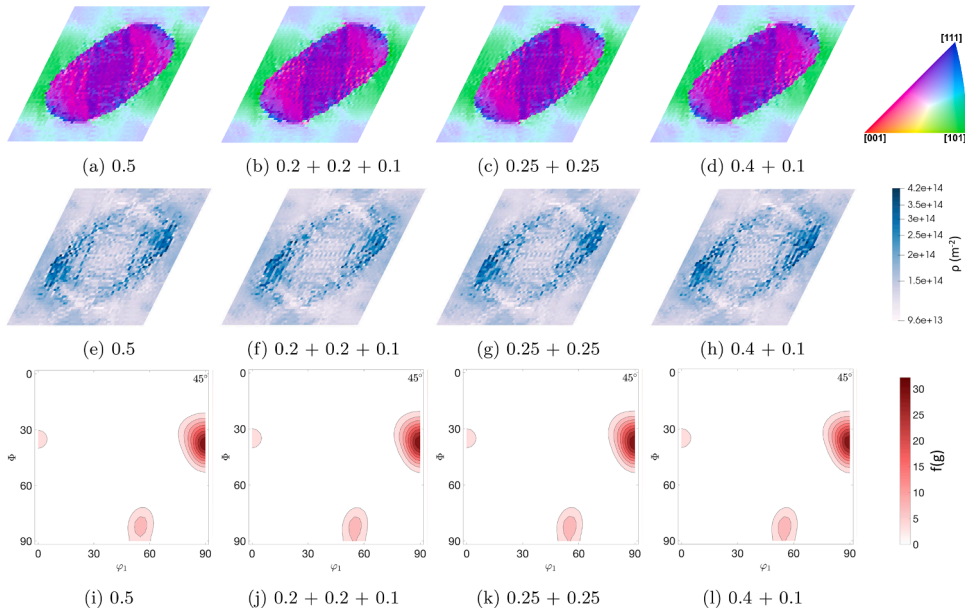


Fig. 10. Influence of the remeshing strategy on the simulation outputs. (a-d) IPF color maps parallel to the vertical direction, (e-h) mobile dislocation density maps, and (i-l) orientation density  $f(g)$  maps obtained from the ODFs. The results are for the example presented in Fig. 1(c).

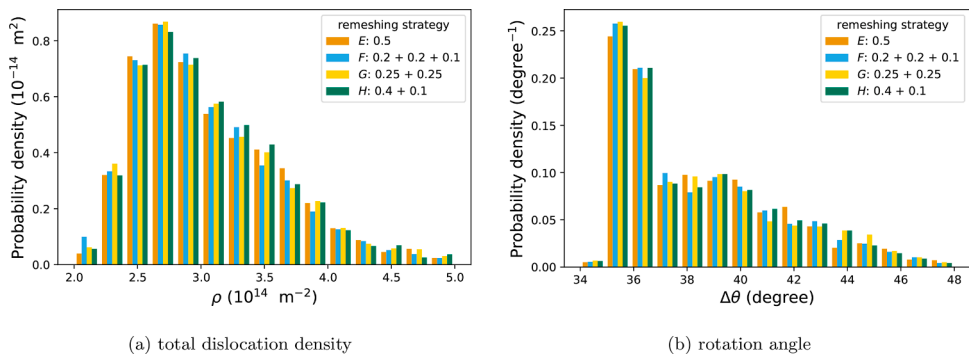


Fig. 11. Influence of the remeshing strategy on the distribution of (a) total dislocation density, (b) rotation angle. Strategy E show the outputs for the case without remeshing.

coordinate directions at any remeshing step. This ability to adjust the resolution is essential for accurate and efficient simulation of large deformations. This section explains the importance and the primary capabilities of the adaptivity scheme and discusses its influence on the level of detail captured in a large deformation crystal plasticity simulation.

Fig. 12 (a) shows the RVE presented in Fig. 1(a) after 75% thickness reduction. For this case, the mesh replacement method is used

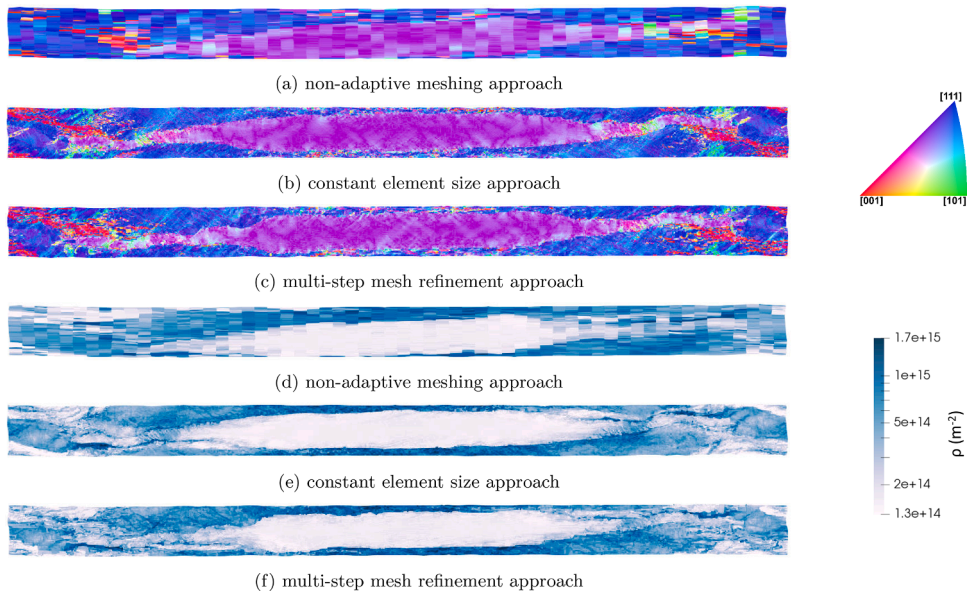
without the adaptive scheme, i.e. the mesh density is kept constant as  $60 \times 60$ . The element size in the loading direction decreases with increasing the deformation, while the element is elongated in the stretching direction. Therefore, the element becomes rectangular, and the element aspect ratio, the ratio of the element size in the stretching direction to the element size in the compression direction, considerably increases. Although a small aspect ratio at small strain is not an issue, this can introduce inaccuracies at large deformations when the aspect ratio becomes too large. For example, for the RVE subjected to 75% thickness reduction, the elements aspect ratio is around 16. Similarly, the aspect ratio increases to 45 for an RVE subjected to 85% thickness reduction. Such extensively elongated elements introduce errors in the simulation. In addition, an element represents the average response of a section in the discretized space. Therefore, if the element size is larger than the localized features, such as shear bands, it will capture only the homogenized behavior and not the morphology of the localized deformation. As a result, highly elongated elements can prevent strain localization from occurring. Hence, the ability to adjust the resolution according to the problem is crucial for large deformation simulations. In the following, we present two different strategies for adjusting the resolution during deformation.

#### 4.2.1. Constant element size approach

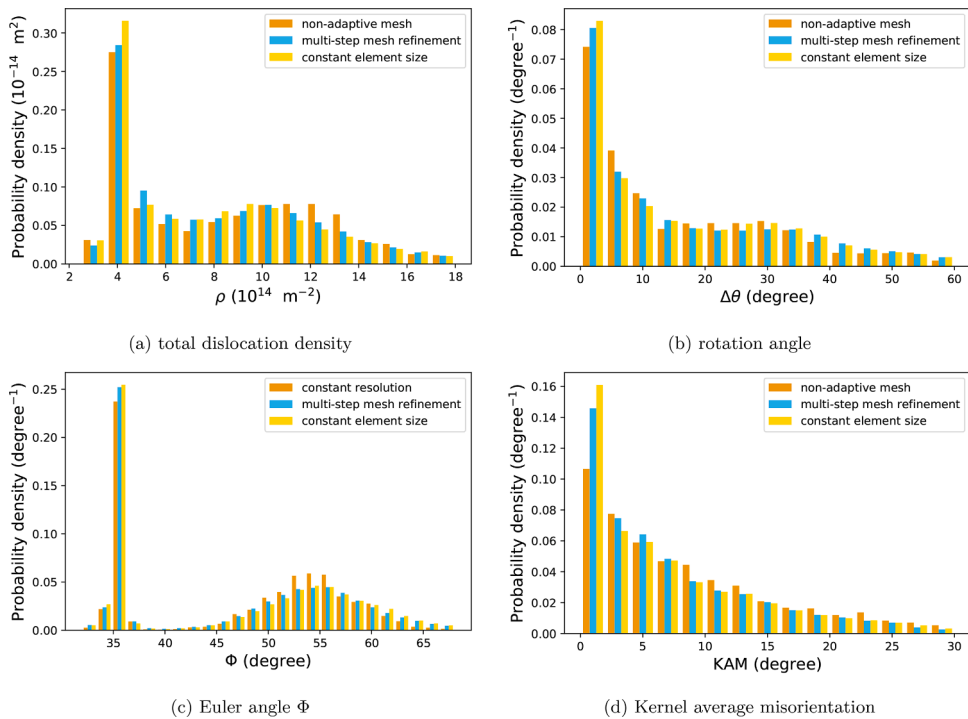
The first approach, which we call the constant element size approach, is based on keeping the element size in all directions constant by adaptively changing the number of elements in different directions during the simulation. This implies decreasing the number of elements in the compression direction and increasing the number of elements in the stretching direction. Using this adaptive meshing method, the number of elements remains approximately constant throughout the simulation. This approach's success requires an initial high mesh density since it results in a significant decrease in the number of elements in the compression direction. However, once the starting mesh density is adequately selected, one can reach the desired mesh density at the end of the simulation.

Fig. 12 (b) and Fig. 12(e) show the results obtained using the constant element size approach. The initial number of elements are  $240 \times 240$ , which are adjusted adaptively to  $873 \times 66$  after 75% thickness reduction. It can be seen that the adaptivity helps to adjust the resolution and to prevent the elements from becoming extensively elongated. More importantly, comparing Fig. 12(a) and Fig. 12 (b) or Fig. 12(d) and Fig. 12(e) reveals that the amount of detail and deformation heterogeneity captured using the adaptive simulation is considerably higher than for the non-adaptive simulation. The elongated elements in the non-adaptive simulation prevent the formation of sharply localized features during the deformation.

Fig. 13 shows the distribution of the total dislocation density, rotation angle, Euler angle  $\Phi$ , and Kernel average misorientation (KAM). For calculating the KAM of a simulation point, first, the disorientations, i.e. the misorientation considering the cubic symmetry of the material, between the point and all neighboring points are calculated. Then, the average value is calculated. Despite the apparent differences between the amount of localized detail captured using the adaptive and non-adaptive simulations, there are some large-scale similarities between the distributions of outputs. This similarity is pronounced for variables such as dislocation density, rotation angle, and Euler angle  $\Phi$  with the Kolmogorov-Smirnov values of 0.072, 0.046, and 0.061, respectively. However, the similarity lessens for the KAM, with a Kolmogorov-Smirnov value of 0.131. The KAM is a measure of local misorientation, and its value depends



**Fig. 12.** Effect of adaptive remeshing and mesh refinement on the simulation outputs; (a-c) IPF color maps parallel to the loading (vertical) direction, (d-f) mobile dislocation density maps. For the non-adaptive simulation, the initial mesh density of  $60 \times 60$  is kept constant during the deformation, which results in highly elongated elements at large deformations. For the multi-step mesh refinement the number of elements is gradually increased during the deformation to  $777 \times 60$ , while for the case of the constant element size approach, the initial number of elements is  $240 \times 240$ , which is adjusted gradually to  $873 \times 66$ . The results are shown for the example presented in Fig. 1(a) subjected to 75% thickness reduction.



**Fig. 13.** Effect of adaptive remeshing and mesh refinement on the distribution of (a) total dislocation density, (b) rotation angle, (c) Euler angle  $\Phi$ , (d) Kernel average misorientation. The results are shown for the cases presented in Fig. 12.

on the local variation of the orientation of a point and its neighboring points. Therefore, as is expected, its distribution is affected more strongly by the resolution of the simulation.

**4.2.2. Multi-step mesh refinement method**

The constant element size approach results in a significant decrease in the number of elements in the compression direction, and its success requires an initially high mesh resolution. As a result, it is not computationally efficient for high-resolution crystal plasticity problems. Here, we introduce a second adaptivity approach, which is named the multi-step mesh refinement method. The idea behind this approach is to keep the number of elements in the compression direction constant, i.e. 60 elements for the current example. The number of elements in the stretching direction is then adjusted accordingly to keep the elements close to cube-shaped. Accordingly, the multi-step mesh refinement approach leads to a gradual rise in the number of points and the simulation resolution during the deformation. Fig. 12(c) and Fig. 12(f) show the results when this adaptive scheme is used, and the number of elements in different directions are gradually increased to  $777 \times 60$ . We recommend keeping the element number in the most compressed direction constant to ensure a minimum information loss during mapping with a minimal increase in the simulation points. It should be noted that using extra elements in the most compressed direction may improve the mapping, but it also inefficiently increases the computational cost.

The results from the two adaptive strategies are very similar. However, the computational cost of the multi-step refinement approach is around 18 times less than the constant element size approach. Using the multi-step refinement approach, one can start the

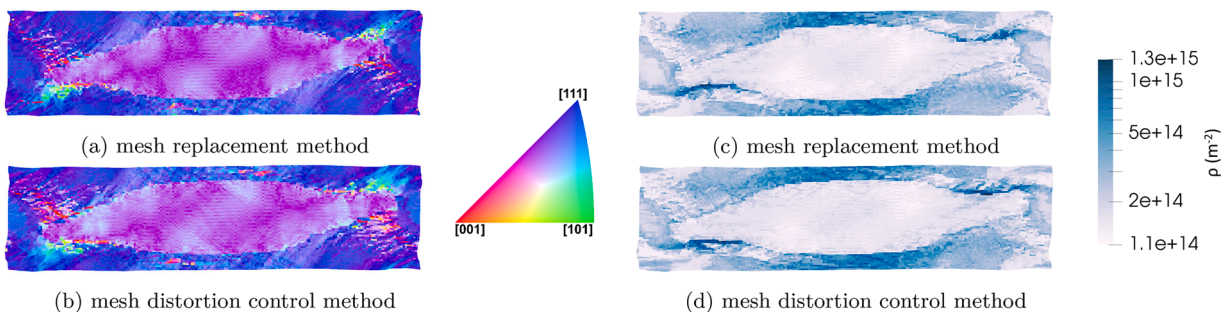


**Fig. 14.** Effect of remeshing approach on the simulation outputs. The results are shown for the bicrystal example presented in Fig. 1(a) subjected to 50% thickness reduction. (a-b) IPF color maps parallel to the loading (vertical) direction, (c-d) mobile dislocation density maps.

simulation with a low but reasonable resolution and gradually increase the resolution to the desired one at the end of the simulation. As a result, a significant portion of the simulation will be done with a lower resolution, which substantially reduces the computational cost and boosts the simulation speed. This is essentially important for high-resolution crystal plasticity simulations, which are, in general, time-consuming.

#### 4.3. Comparing mesh replacement method and mesh distortion control method

The two remeshing algorithms proposed in this study are compared in Fig. 14. The results are for the RVE in Fig. 1(a) subjected to 50% thickness reduction. The results obtained from the two approaches are in good agreement. The Kolmogorov-Smirnov values for the distribution of the total dislocation density, rotation angle, Euler angle  $\Phi$ , and Kernel average misorientation are 0.052, 0.064, 0.059, and 0.038, respectively. The distributions of the total dislocation density and the rotation angle are shown in Fig. 15. It can be seen that the differences belong mainly to the lower tail of the distributions. Besides, there is a good agreement between the distributions for the Kernel average misorientation.

We observed that the mesh distortion control method's computational cost, especially at higher strains, is significantly higher than the mesh replacement method. For example, the total number of iterations required to reach 50% thickness reduction for the mesh distortion control method is around twice that of the mesh replacement method. This ratio is four times higher to reach 70% thickness reduction. Since the difference between outputs is subtle, for cases where both approaches are applicable, e.g. compression and tension loading, one can save a substantial amount of computational cost using the mesh replacement method. The mesh distortion control method's main advantage is for cases where the mesh replacement method is not applicable, as explained in the next section.

#### 4.4. Shear deformation

Shear deformation takes place in many industrial processes, e.g. during the rolling near the surface (Segurado et al., 2012), asymmetric rolling (Ren et al., 2021), or extrusion and reversible rolling (Pérocheau and Driver, 2000). However, performing remeshing when the configuration is subjected to a loading condition that involves shearing is challenging. This is because it is difficult for such loading conditions to preserve the periodicity requirements, see Fig. 16(a). Frydrych et al. (2019) performed the remeshing for an RVE under simple shear according to an approach based on the structure periodicity, as shown in Fig. 16(b). This approach requires the remeshing to be performed at a particular strain point at which the corners of the generated cube-shape configurations coincide precisely with the corners of the deformed configuration.

Although this approach can be used for simulating large shear deformation under periodic boundary conditions, it has two main drawbacks: Firstly, the application of this approach is limited to structures under simple shear. In other words, this approach cannot be used to simulate mixed loading conditions, where the shear load is applied simultaneously with another type of load, such as compression or tension. Secondly, the remeshing approach needs to be performed at a particular strain point. Therefore, if the mesh distortion becomes too large and the simulation fails before this specific strain point, the remeshing cannot be applied.

The mesh distortion control method, see Section 3.1.2 for detail, can overcome the challenges related to loading conditions involving shearing. According to this approach, the undistorted mesh is achieved by maintaining the spatially homogeneous part of the deformation and only removing the fluctuating part of the deformation. This means that the applied boundary conditions for the restart analysis are defined according to the initial geometry and similar to when there is no remeshing. As a result, independent of the remeshing strain and the loading type, the periodicity is always preserved, and this approach can be used for any desired loading conditions. Fig. 17 shows an RVE subjected to a mixed loading condition, i.e. compression and shear deformation. Here, the RVE presented in Fig. 1(a) is subjected to 75% thickness reduction and 20% shearing.

#### 4.5. High-resolution 3D simulations: grain shape effect

While the influence of crystallographic orientation/texture is extensively discussed in the literature, less attention has been paid to the effect of the grain shape and its neighboring conditions on the plastic deformation heterogeneity. One reason for this might be the computational/experimental efforts that are required for systematic investigations in this enlarged parameter space. From the computational point of view, studying the grain shape requires a high-resolution crystal plasticity simulation. The first hurdle of high-resolution crystal plasticity simulations is the significant increase in the computational cost with an increase in the simulation resolution. This is a limiting factor in the number of elements per grain and the number of grains used in a polycrystal simulation. The second problem is that since a higher resolution simulation allows capturing more detailed localized deformation features, as discussed earlier, it is prone to earlier convergence issues.

The remeshing approaches introduced in this study allow us to overcome the convergence issues. Furthermore, the multi-step mesh refinement approach suggested in Section 4.2 provides a computationally efficient strategy to simulate large-deformation high-resolution problems. In this section, the merits of this combined modeling strategy in investigating the grain shape effect are shown using a high-resolution bicrystal example. For this purpose, we use an RVE similar to the one presented in Fig. 1(a). However, for the current investigation, the diameter of the central grain is reduced to 60% of the configuration's thickness. Fig. 18(a) and Fig. 18(d) show respectively the IPF color map parallel to the loading direction and the mobile dislocation density map for this RVE. Here, only one element is used in the transverse direction.

In the next step, the RVE is converted to a full 3D model by extruding the quasi-3D RVE in the transverse direction to generate a cubic RVE. In this case, the central grain has a cylindrical shape. Fig. 18(b) shows the results for the mid-surface obtained using this 3D

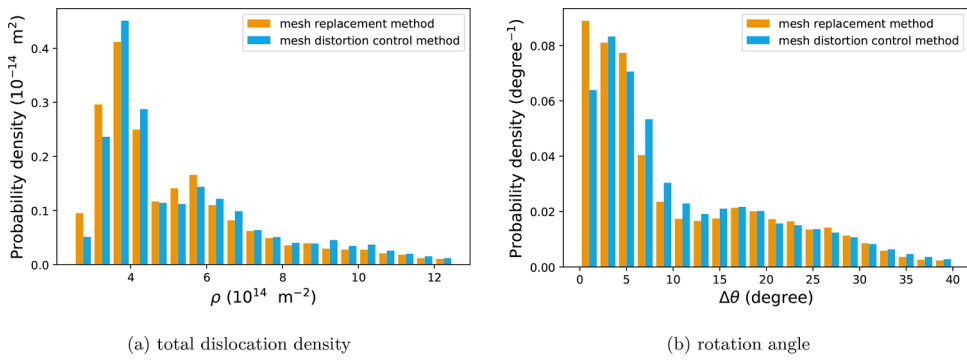


**Fig. 15.** Effect of remeshing approach on the distribution of (a) total dislocation density, (b) rotation angle. The results are shown for the cases presented in Fig. 14.

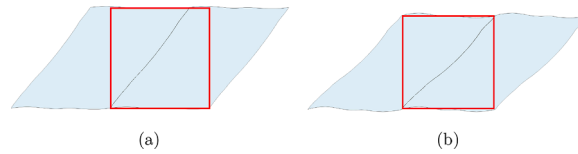


**Fig. 16.** A schematic plot showing the challenges of preserving the periodicity requirements of the configuration during the remeshing for a configuration subjected to simple shear. The deformed RVE and a copy of it are shown in light blue. The red square shows the newly generated RVE after remeshing. (a) The periodicity requirements are violated during remeshing when the RVE is subjected to a shear strain of 0.8. (b) To preserve the periodicity requirements, the remeshing needs to be performed at a particular strain point, i.e. a shear strain of 1 for the depicted example. As a result, this approach is limited to structures under simple shear. The mesh distortion control method, see Section 3.1.2, can overcome the challenges related to loading conditions involving shearing.

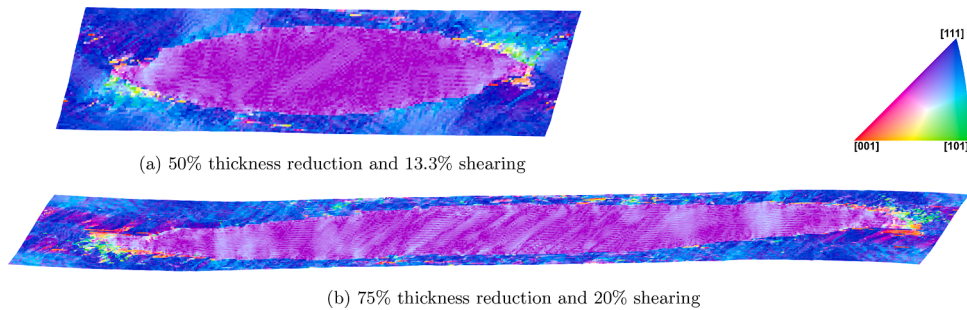


**Fig. 17.** The mesh distortion control method is employed to simulate a structure subjected to mixed compression and shear loading. The figures show IPF color maps parallel to the vertical direction for the example presented in Fig. 1(a).

simulation after 75% thickness reduction. The initial number of elements for this simulation is  $60 \times 30 \times 60$ , and is increased gradually to  $777 \times 109 \times 60$  during the 75% thickness reduction. In general, both simulations give the same response. The main difference between the two simulations is the slightly sharper localized deformation in the 2D simulation. Moreover, we observed that the difference between the results at the surface of the 3D simulation and the quasi-3D simulation is more pronounced.

In the final step, the effect of substituting the cylindrical grain with a spherical grain with the same diameter is investigated. Fig. 18 (c) and Fig. 18(e) show respectively the IPF color map parallel to the loading direction and the mobile dislocation density map after 75% thickness reduction. The results are shown at the mid-surface in the transverse direction. The texture and microstructures developed during the deformation are visibly altered by the change in the grain shape. Therefore, though the quasi-3D simulation is able to reproduce the 3D results for the exactly equivalent microstructure, it is unable to incorporate the actual effect of grain morphology. The distributions of the total dislocation density and rotation angle for the three discussed cases are shown in Fig. 19.

#### 4.6. High-resolution 3D simulations: application to polycrystals

In this section, the remeshing methodology is applied to perform a high-resolution large-deformation crystal plasticity simulation on a 3D polycrystal example. For this purpose, the simulation is carried out on a polycrystal configuration made of 38 randomly

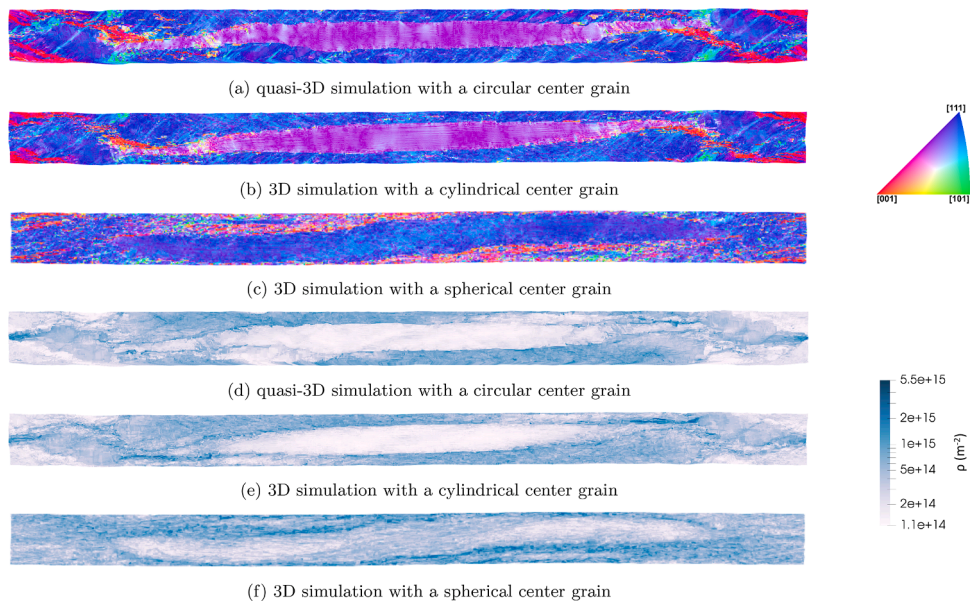


**Fig. 18.** Effect of grain shape on the microstructure evolution. The results are shown for a bicrystal example similar to the one presented in Fig. 1(a), but with a slightly smaller center grain. The RVE is subjected to 75% thickness reduction. (a-c) IPF color maps parallel to the loading (vertical) direction, (d-f) mobile dislocation density maps.

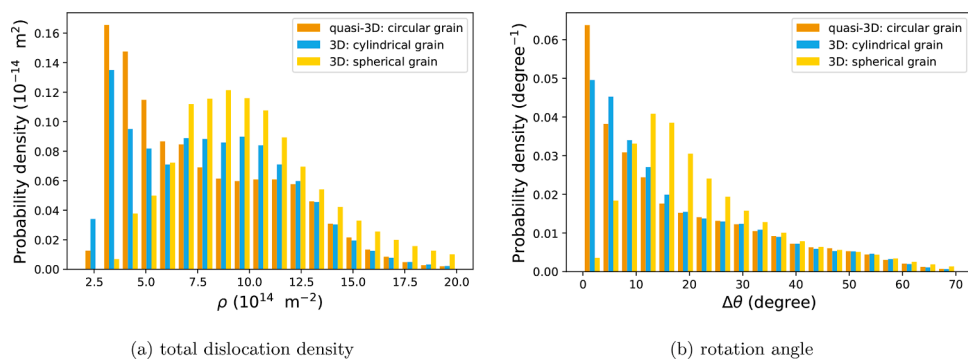
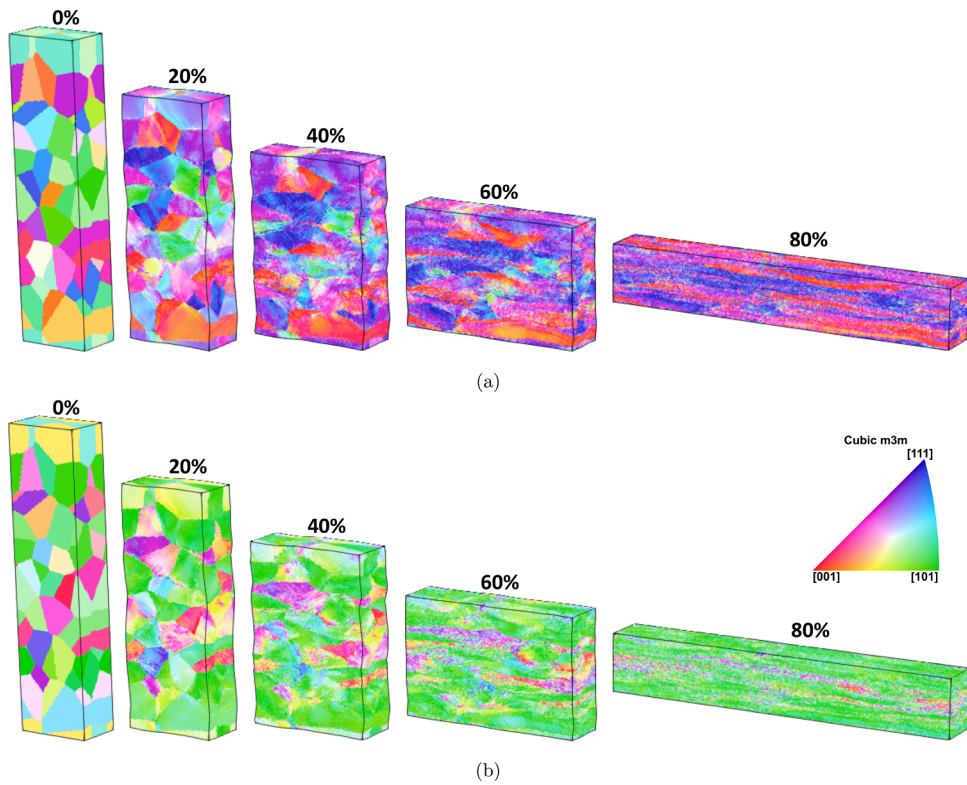


**Fig. 19.** Effect of grain shape on the distribution of (a) total dislocation density, (b) rotation angle. The results are shown for the cases presented in Fig. 18.

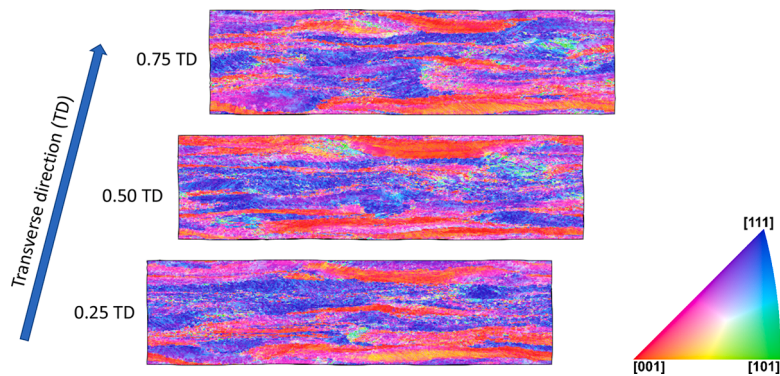
oriented grains, as illustrated in Fig. 20. The properties used in the crystal plasticity simulations are similar to those proposed for IF-steel in (Sedighiani et al., 2021). The RVE is subjected to plane-strain compression up to a thickness reduction of 80%. The initial number of elements at the beginning of the deformation is  $80 \times 48 \times 320$ . The mesh density is gradually increased to  $1314 \times 48 \times 320$  during the deformation, i.e. the number of elements is increased by a factor of 16.

Fig. 20 shows the IPF color maps parallel to the loading (vertical) and stretching (horizontal) directions after 20, 40, 60, and 80% thickness reduction. It can be seen how the plastic deformation leads to changes in the grains' orientation and, consequently, to the development of deformation textures. As the load increases, a strong  $\alpha$ -fiber texture (RD||<110>) and a comparably weaker  $\gamma$ -fiber (ND||<111>) texture are developed, typical for IF-steel (Hutchinson 1999; Kestens and Pircgazi 2016).

The IPF color maps parallel to the loading (vertical) direction for three different sections in the transverse direction are shown in Fig. 21. The results are for 75% thickness reduction. It can be seen from this figure and Fig. 20 how the originally uniformly orientated crystals are subdivided and rotated into portions with different orientations. In other words, the heterogeneous deformations within individual grains result in the grain fragmentation and the development of smaller grains separated by high-angle misorientation boundaries. The plastic heterogeneity of the deformation depends on many factors, such as the orientation distribution, grain shape, or grain size. However, in general, the heterogeneity of the deformation is more pronounced in the  $\gamma$ -fiber grains. The qualitative resemblance of these results with experimentally observed electron backscattered diffraction (EBSD) maps is striking. As an example, an EBSD measurement for a cold-rolled IF-steel sample after 75% thickness reduction is shown in Fig. 22. It should be noted that the experimental data provided here does not represent the same sample as the simulated one. A detailed comparison between the



**Fig. 20.** IPF color maps parallel to the (a) loading (vertical) direction (b) stretching (horizontal) direction at different thickness reductions for a 3D high-resolution polycrystal made of 38 randomly oriented grains.



**Fig. 21.** IPF color maps parallel to the loading (vertical) direction at different transverse positions for the same RVE presented in Fig. 20 subjected to 75% thickness reduction.

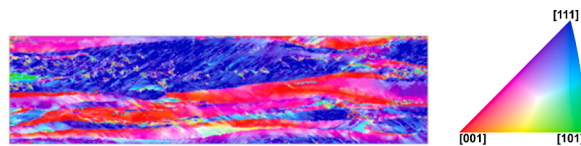


**Fig. 22.** Electron backscattered diffraction (EBSD) measurements of a cold rolled IF steel sample after 75% thickness reduction. The figure shows the IPF color map parallel to the normal (loading) direction for a section of  $60 \times 230 \mu\text{m}^2$ .

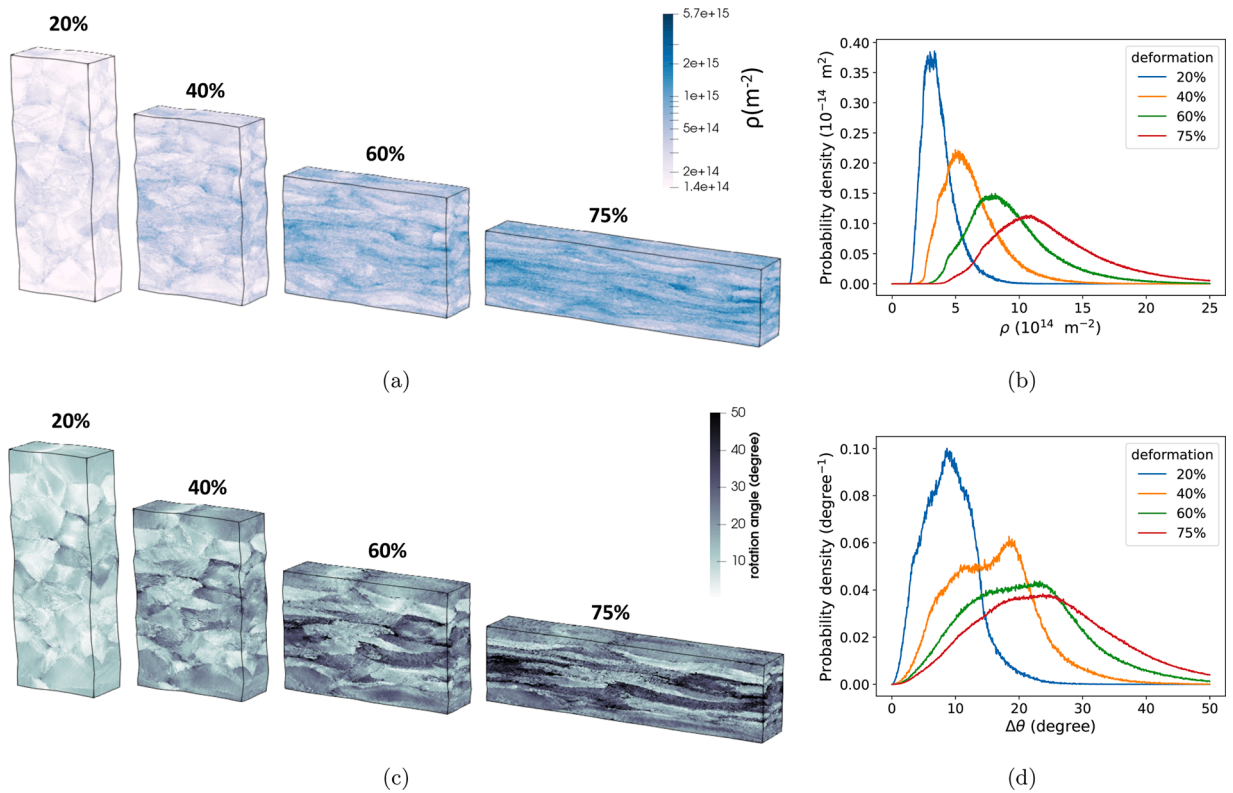


**Fig. 23.** Deformation heterogeneity in a 3D high-resolution polycrystal made of 38 randomly oriented grains at different thickness reductions, (a) evolution of the dislocation density, (b) the corresponding distributions. (c) evolution of the rotation angle, see Eq. 10, (d) the corresponding distributions.

simulation results and the EBSD data will be provided in a subsequent paper focused on microstructure evolution in IF-steel.

Fig. 23 shows the development of the dislocation density and the rotation angle at different thickness reduction levels. The results reveal that the development of dislocation density and rotation angle is different based on the crystals' orientation, and their distributions are inhomogeneous at all strain levels.

## 5. Conclusions

Problems involving the deformation of solid materials are usually formulated in a way that the mesh is attached to the deformable body and deforms with a change in the shape of the material. This means that the mesh gets distorted due to the heterogeneity of the deformation. In this study, two different approaches to overcome the mesh distortion problem at large strains were proposed, i.e. the mesh replacement method and the mesh distortion control method. The accuracy of the two methods was examined using different test cases designed to evaluate the various steps involved. It was shown that both approaches enable conducting high-resolution large-deformation crystal plasticity simulations and overcoming the associated mesh distortion problem due to the strain localization.

In the mesh replacement method, the deformed configuration with the distorted mesh is replaced by a new configuration with an undistorted mesh. Therefore, it can be stated that the mesh replacement method is like starting a new analysis in which the initial state of the model is obtained from a different analysis. In the mesh distortion control method, the undistorted mesh is achieved by removing the fluctuating part of the deformation and keeping the homogeneous part of the deformation. Hence, contrary to the mesh replacement method, this approach requires finding a new equilibrium state for the smoothed mesh. This leads to a higher computational cost for the mesh distortion control method, especially at large strains. Since no significant difference between the results from the two remeshing approaches was observed, a substantial amount of computational cost can be saved using the mesh replacement method. However, in the case of using periodic boundary conditions, it is challenging to preserve the periodicity requirements for some loading conditions, e.g. loadings involving shear. For such complex loading conditions, the mesh distortion method was proposed. Since the homogeneous part of the deformation is retained during the undistorted mesh generation for the mesh distortion control method, the periodicity requirements are always conserved regardless of the loading condition. Therefore, the mesh distortion control method's main advantage is that it enables remeshing in situations where the periodicity of the geometry would be broken by the mesh replacement method.

A global adaptive scheme was implemented for both remeshing approaches, allowing to update the number of elements in the three coordinate directions at any remeshing steps. This adaptive scheme is important to prevent the elements' aspect ratio from becoming

too large. Besides, a multi-step mesh refinement approach was suggested for efficient simulation of large-deformation high-resolution crystal plasticity problems. It was shown that this adaptive meshing strategy can be used, for example, to capture the effect of grain shape on the plastic deformation heterogeneity.

Finally, the mesh replacement method was employed to carry out a 3D high-resolution large-deformation crystal plasticity simulation. It was observed that the remeshing approaches allow capturing the development of deformation heterogeneity and strain localization in polycrystals, e.g. in-grain orientation spread. Such detailed high-resolution large-deformation simulations can be used to thoroughly analyze how, for example, deformation heterogeneity or in-grain orientation spread depends on the crystal orientation, neighbor grains, or any other relevant factors. Moreover, capturing such localized details enables modeling subsequent processes, such as recrystallization, which are dependent on the formation of these localized deformation features.

## Data availability

The remeshing approaches have been implemented into DAMASK ([damask.mpie.de](https://damask.mpie.de)) and are available for free at [git.damask.mpie.de](https://git.damask.mpie.de).

## CRediT authorship contribution statement

**Karo Sedighiani:** Conceptualization, Methodology, Software, Validation, Formal analysis, Investigation, Writing – original draft, Visualization. **Vitesh Shah:** Visualization, Validation, Investigation, Writing – review & editing. **Konstantina Traka:** Visualization, Validation, Investigation, Writing – review & editing. **Martin Diehl:** Methodology, Software, Data curation, Writing – review & editing, Visualization, Supervision. **Franz Roters:** Software, Resources, Data curation, Writing – review & editing, Supervision. **Jilt Sietsma:** Writing – review & editing, Supervision, Project administration, Funding acquisition. **Dierk Raabe:** Resources, Writing – review & editing, Supervision, Project administration, Funding acquisition.

## Declaration of Competing Interest

The authors declare that they have no known competing financial interests or personal relationships that could have appeared to influence the work reported in this paper.

## Acknowledgments

This research was carried out under project number S41.5.15572a in the framework of the Partnership Program of the Materials innovation institute M2i ([www.m2i.nl](http://www.m2i.nl)) and the Technology Foundation TTW ([www.stw.nl](http://www.stw.nl)), which is part of the Netherlands Organization for Scientific Research ([www.nwo.nl](http://www.nwo.nl)).

## References

- Alaneme, K.K., Okotete, E.A., 2019. Recrystallization mechanisms and microstructure development in emerging metallic materials: A review. *Journal of Science: Advanced Materials and Devices* 19–33. <https://doi.org/10.1016/j.jsamd.2018.12.007>.
- Bate, P., 1999. Modelling deformation microstructure with the crystal plasticity finite-element method. *Philosophical Transactions of the Royal Society A: Mathematical, Physical and Engineering Sciences* 357 (1756). <https://doi.org/10.1098/rsta.1999.0391>.
- Beaudoin, A.J., Mecking, H., Kocks, U.F., 1996. Development of localized orientation gradients in fcc polycrystals. *Philosophical Magazine A: Physics of Condensed Matter, Structure, Defects and Mechanical Properties* 73 (6). <https://doi.org/10.1080/01418619608242998>.
- Cappola, J., Stinville, J.C., Charpagne, M., Callahan, P.G., Echlin, M.P., Pollock, T.M., Pilchak, A., Kasemer, M., 2021. On the Localization of Plastic Strain in Microtextured Regions of Ti-6Al-4V. *Acta Materialia* 204, 116492. <https://doi.org/10.1016/j.actamat.2020.116492>.
- Chen, L., Chen, J., Lebensohn, R.A., Ji, Y.Z., Heo, T.W., Bhattacharyya, S., Chang, K., Mathaudhu, S., Liu, Z.K., Chen, L.Q., 2015. An integrated fast Fourier transform-based phase-field and crystal plasticity approach to model recrystallization of three dimensional polycrystals. *Computer Methods in Applied Mechanics and Engineering* 285, 829–848. <https://doi.org/10.1016/j.cma.2014.12.007>.
- Chen, L., James Edwards, T.E., Di Giocchino, F., Clegg, W.J., Dunne, F.P.E., Pham, M.S., 2019. Crystal plasticity analysis of deformation anisotropy of lamellar TiAl alloy: 3D microstructure-based modelling and in-situ microcompression. *International Journal of Plasticity* 119. <https://doi.org/10.1016/j.ijplas.2019.04.012>.
- Choi, S., 2003. Simulation of stored energy and orientation gradients in cold-rolled interstitial free steels. *Acta Materialia* 51 (6), 1775–1788. [https://doi.org/10.1016/S1359-6454\(02\)00576-1](https://doi.org/10.1016/S1359-6454(02)00576-1).
- Connolly, D.S., Kohar, C.P., Muhammad, W., Hector, L.G., Mishra, R.K., Inal, K., 2020. A coupled thermomechanical crystal plasticity model applied to Quenched and Partitioned steel. *International Journal of Plasticity* 133, 102757. <https://doi.org/10.1016/j.ijplas.2020.102757>.
- Dao, M., Lit, M., 2001. A micromechanics study on strain-localization-induced fracture initiation in bending using crystal plasticity models. *Philosophical Magazine A: Physics of Condensed Matter, Structure, Defects and Mechanical Properties* 81 (8). <https://doi.org/10.1080/01418610108216649>.
- Dequiedt, J.L., Denoual, C., 2021. Localization of plastic deformation in stretching sheets with a crystal plasticity approach: Competition between weakest link and instable mode controlled process. *International Journal of Solids and Structures* 210–211. <https://doi.org/10.1016/j.ijsolstr.2020.11.021>.
- Diard, O., Leclercq, S., Rousellier, G., Caillaud, G., 2005. Evaluation of finite element based analysis of 3D multicrystalline aggregates plasticity Application to crystal plasticity model identification and the study of stress and strain fields near grain boundaries. *International Journal of Plasticity* 21 (4), 691–722. <https://doi.org/10.1016/j.ijplas.2004.05.017>.
- Diehl, M., An, D., Shanthraj, P., Zaeferrer, S., Roters, F., Raabe, D., 2017. Crystal plasticity study on stress and strain partitioning in a measured 3D dual phase steel microstructure. *Physical Mesomechanics* 20 (3). <https://doi.org/10.1134/S1029959917030079>.
- Diehl, M., Groeber, M., Haase, C., Molodov, D.A., Roters, F., Raabe, D., 2017. Identifying Structure-Property Relationships Through DREAM.3D Representative Volume Elements and DAMASK Crystal Plasticity Simulations: An Integrated Computational Materials Engineering Approach. *JOM* 69 (5). <https://doi.org/10.1007/s11837-017-2303-0>.
- Diehl, M., Kühbach, M., 2020. Coupled experimental-computational analysis of primary static recrystallization in low carbon steel. *Modelling and Simulation in Materials Science and Engineering* 28 (1). <https://doi.org/10.1088/1361-651X/ab51bd>.

- Diehl, M., Niehuesbernd, J., Bruder, E., 2019. Quantifying the contribution of crystallographic texture and grain morphology on the elastic and plastic anisotropy of bcc steel. *Metals* 9 (12). <https://doi.org/10.3390/met9121252>.
- Diehl, M., Wicke, M., Shanthraj, P., Roters, F., Brueckner-Foitz, A., Raabe, D., 2017. Coupled Crystal Plasticity-Phase Field Fracture Simulation Study on Damage Evolution Around a Void: Pore Shape Versus Crystallographic Orientation. *Jom* 69 (5), 872–878. <https://doi.org/10.1007/s11837-017-2308-8>.
- Eisenlohr, P., Diehl, M., Lebensohn, R., Roters, F., 2013. A spectral method solution to crystal elasto-viscoplasticity at finite strains. *International Journal of Plasticity* 46, 37–53. <https://doi.org/10.1016/j.ijplas.2012.09.012>.
- Forest, S., 1998. Modeling slip, kink and shear banding in classical and generalized single crystal plasticity. *Acta Materialia* 46 (9). [https://doi.org/10.1016/S1359-6454\(98\)00012-3](https://doi.org/10.1016/S1359-6454(98)00012-3).
- Frydrych, K., Kowalczyk-Gajewska, K., Prakash, A., 2019. On solution mapping and remeshing in crystal plasticity finite element simulations: application to equal channel angular pressing. *Modelling and Simulation in Materials Science and Engineering* 27 (7). <https://doi.org/10.1088/1361-651X/ab28e3>.
- Gierden, C., Kochmann, J., Waimann, J., Kinner-Becker, T., Sölter, J., Svendsen, B., Reese, S., 2021. Efficient two-scale FE-FFT-based mechanical process simulation of elasto-viscoplastic polycrystals at finite strains. *Computer Methods in Applied Mechanics and Engineering* 374, 113566. <https://doi.org/10.1016/j.cma.2020.113566>.
- Hughes, D.A., Hansen, N., 2000. Microstructure and strength of nickel at large strains. *Acta Materialia* 48 (11), 2985–3004. [https://doi.org/10.1016/S1359-6454\(00\)00082-3](https://doi.org/10.1016/S1359-6454(00)00082-3).
- Hutchinson, B., 1999. Deformation microstructures and textures in steels. *Philosophical Transactions of the Royal Society A: Mathematical, Physical and Engineering Sciences* 357 (1756), 1471–1485. <https://doi.org/10.1098/rsta.1999.0385>.
- Jalili, M., Soltani, B., 2020. Investigation of the micromechanisms of strain localization formation in AZ31 Mg alloy: A mesoscale 3D full-field crystal plasticity computational homogenization study. *European Journal of Mechanics, A/Solids* 80, 103903. <https://doi.org/10.1016/j.euromechsol.2019.103903>.
- Jia, N., Roters, F., Eisenlohr, P., Kords, C., Raabe, D., 2012. Non-crystallographic shear banding in crystal plasticity FEM simulations: Example of texture evolution in  $\alpha$ -brass. *Acta Materialia* 60 (3). <https://doi.org/10.1016/j.actamat.2011.10.047>.
- Kanjaria, A.K., Van Houtte, P., Delannay, L., 2010. Assessment of plastic heterogeneity in grain interaction models using crystal plasticity finite element method. *International Journal of Plasticity* 26 (8). <https://doi.org/10.1016/j.ijplas.2009.05.005>.
- Kasemer, M., Dawson, P., 2020. A finite element methodology to incorporate kinematic activation of discrete deformation twins in a crystal plasticity framework. *Computer Methods in Applied Mechanics and Engineering* 358. <https://doi.org/10.1016/j.cma.2019.112653>.
- Kestens, L.A.L., Pirgazi, H., 2016. Texture formation in metal alloys with cubic crystal structures. *Materials Science and Technology* 32 (13), 1303–1315. <https://doi.org/10.1080/02670836.2016.1231746>.
- Khadyko, M., Dumoulin, S., Hopperstad, O.S., 2016. Texture gradients and strain localisation in extruded aluminium profile. *International Journal of Solids and Structures* 97, 239–255. <https://doi.org/10.1016/j.ijsolstr.2016.07.024>.
- Kim, D., Woo, W., Park, W., Im, Y., Rollett, A., 2017. Mesoscopic coupled modeling of texture formation during recrystallization considering stored energy decomposition. *Computational Materials Science* 129. <https://doi.org/10.1016/j.commatsci.2016.11.048>.
- Kim, D.K., Kim, J.M., Park, W.W., Lee, H., Im, Y.T., Lee, Y.S., 2015. Three-dimensional crystal plasticity finite element analysis of microstructure and texture evolution during channel die compression of if steel. *Computational Materials Science* 100 (PA), 52–60. <https://doi.org/10.1016/j.commatsci.2014.09.032>.
- Kweon, S., Raja, D.S., 2017. Comparison of anisotropy evolution in BCC and FCC metals using crystal plasticity and texture analysis. *European Journal of Mechanics, A/Solids* 62, 22–38. <https://doi.org/10.1016/j.euromechsol.2016.11.002>.
- Liang, Y., He, Q., Jiang, S., Zhao, C., 2020. Investigation on Texture Evolution Mechanism of NiTiFe Shape Memory Alloy Under Plane Strain Compression. *Metals and Materials International*. <https://doi.org/10.1007/s12540-020-00741-6>.
- Lim, H., Battaile, C.C., Bishop, J.E., Foulk, J.W., 2019. Investigating mesh sensitivity and polycrystalline RVEs in crystal plasticity finite element simulations. *International Journal of Plasticity* 121, 101–115. <https://doi.org/10.1016/j.ijplas.2019.06.001>.
- Ma, A., Roters, F., 2004. A constitutive model for fcc single crystals based on dislocation densities and its application to uniaxial compression of aluminium single crystals. *Acta Materialia* 52 (12), 3603–3612. <https://doi.org/10.1016/j.actamat.2004.04.012>.
- Ma, A., Roters, F., Raabe, D., 2006. A dislocation density based constitutive model for crystal plasticity FEM including geometrically necessary dislocations. *Acta Materialia* 54 (8), 2169–2179. <https://doi.org/10.1016/j.actamat.2006.01.005>.
- Maneevongvatana, S., Mount, D., 2001. On the efficiency of nearest neighbor searching with data clustered in lower dimensions. *Lecture Notes in Computer Science (including subseries Lecture Notes in Artificial Intelligence and Lecture Notes in Bioinformatics)*, 2073. [https://doi.org/10.1007/3-540-45545-0\\_96](https://doi.org/10.1007/3-540-45545-0_96).
- Massey, F., 1951. The Kolmogorov-Smirnov Test for Goodness of Fit. *Journal of the American Statistical Association* 46 (253). <https://doi.org/10.1080/01621459.1951.10500769>.
- Traka, K., Sedighiani, K., Bos, C., Lopez, J.G., Angenendt, K., Raabe, D., Sietsma, J., 2021. Topological aspects responsible for recrystallization evolution in an IF-steel sheet - Investigation with cellular-automaton simulations. *Computational Materials Science* 198, 110643. <https://doi.org/10.1016/j.commatsci.2021.110643>.
- van Nuland, T.F., van Dommelen, J.A., Geers, M.G., 2021. Microstructural modeling of anisotropic plasticity in large scale additively manufactured 316L stainless steel. *Mechanics of Materials* 153. <https://doi.org/10.1016/j.mechmat.2020.103664>.
- Oddershede, J., Wright, J.P., Beaudoin, A., Winther, G., 2015. Deformation-induced orientation spread in individual bulk grains of an interstitial-free steel. *Acta Materialia* 85. <https://doi.org/10.1016/j.actamat.2014.11.038>.
- Pérocheau, F., Driver, J.H., 2000. Texture gradient simulations for extrusion and reversible rolling of FCC metals. *International journal of plasticity* 16 (1). [https://doi.org/10.1016/S0749-6419\(99\)00048-0](https://doi.org/10.1016/S0749-6419(99)00048-0).
- Prakash, A., Nöhring, W.G., Lebensohn, R.A., Höppel, H.W., Bitzek, E., 2015. A multiscale simulation framework of the accumulative roll bonding process accounting for texture evolution. *Materials Science and Engineering A* 631, 104–119. <https://doi.org/10.1016/j.msea.2015.02.005>.
- Proudhon, H., Li, J., Wang, F., Roos, A., Chiaruttini, V., Forest, S., 2016. 3D simulation of short fatigue crack propagation by finite element crystal plasticity and remeshing. *International Journal of Fatigue*. Elsevier Ltd, pp. 238–246. <https://doi.org/10.1016/j.ijfatigue.2015.05.022>.
- Quey, R., Dawson, P.R., Barbe, F., 2011. Large-scale 3D random polycrystals for the finite element method: Generation, meshing and remeshing. *Computer Methods in Applied Mechanics and Engineering* 200 (17–20), 1729–1745. <https://doi.org/10.1016/j.cma.2011.01.002>.
- Raabe, D., Zhao, Z., Roters, F., 2004. Study on the orientational stability of cube-oriented FCC crystals under plane strain by use of a texture component crystal plasticity finite element method. *Scripta Materialia* 50 (7). <https://doi.org/10.1016/j.scriptamat.2003.11.061>.
- Ren, X., Huang, Y., Zhang, X., Li, H., Zhao, Y., 2021. Influence of shear deformation during asymmetric rolling on the microstructure, texture, and mechanical properties of the AZ31B magnesium alloy sheet. *Materials Science and Engineering A* 800. <https://doi.org/10.1016/j.msea.2020.140306>.
- Resk, H., Delannay, L., Bernacki, M., Coupeux, T., Logé, R., 2009. Adaptive mesh refinement and automatic remeshing in crystal plasticity finite element simulations. *Modelling and Simulation in Materials Science and Engineering* 17 (7). <https://doi.org/10.1088/0965-0393/17/7/075012>.
- Reuber, C., Eisenlohr, P., Roters, F., Raabe, D., 2014. Dislocation density distribution around an indent in single-crystalline nickel: Comparing nonlocal crystal plasticity finite-element predictions with experiments. *Acta Materialia* 71, 333–348. <https://doi.org/10.1016/j.actamat.2014.03.012>.
- Ritz, H., Dawson, P., 2009. Sensitivity to grain discretization of the simulated crystal stress distributions in FCC polycrystals. *Modelling and Simulation in Materials Science and Engineering* 17 (1). <https://doi.org/10.1088/0965-0393/17/1/015001>.
- Roters, F., Diehl, M., Shanthraj, P., Eisenlohr, P., Reuber, C., Wong, S., Maiti, T., Ebrahimi, A., Hochrainer, T., Fabritius, H., Nikolov, S., Friák, M., Fujita, N., Grilli, N., Janssens, K., Jia, N., Kok, P., Ma, D., Meier, F., Werner, E., Stricker, M., Weygand, D., Raabe, D., 2019. DAMASK - The Düsseldorf Advanced Material Simulation Kit for modeling multi-physics crystal plasticity, thermal, and damage phenomena from the single crystal up to the component scale. *Computational Materials Science* 158, 420–478. <https://doi.org/10.1016/j.commatsci.2018.04.030>.
- Roters, F., Eisenlohr, P., Hantcherli, L., Tjahjanto, D., Bieler, T., Raabe, D., 2010. Overview of constitutive laws, kinematics, homogenization and multiscale methods in crystal plasticity finite-element modeling: Theory, experiments, applications. *Acta Materialia* 58 (4), 1152–1211. <https://doi.org/10.1016/j.actamat.2009.10.058>.

- Sachtler, M., Zhao, Z., Raabe, D., 2002. Experimental investigation of plastic grain interaction. *Materials Science and Engineering A* 336 (1-2), 81–87. [https://doi.org/10.1016/S0921-5093\(01\)01974-8](https://doi.org/10.1016/S0921-5093(01)01974-8).
- Sarma, G., Dawson, P., 1996. Effects of interactions among crystals on the inhomogeneous deformations of polycrystals. *Acta Materialia* 44 (5), 1937–1953. [https://doi.org/10.1016/1359-6454\(95\)00309-6](https://doi.org/10.1016/1359-6454(95)00309-6).
- Savage, D., Beyerlein, I., Mara, N., Vogel, S., McCabe, R., Knezevic, M., 2020. Microstructure and texture evolution in Mg/Nb layered materials made by accumulative roll bonding. *International Journal of Plasticity* 125, 1–26. <https://doi.org/10.1016/j.ijplas.2019.08.015>.
- Sedighiani, K., Diehl, M., Traka, K., Roters, F., Sietsma, J., Raabe, D., 2020. An efficient and robust approach to determine material parameters of crystal plasticity constitutive laws from macro-scale stress-strain curves. *International Journal of Plasticity* 134, 102779. <https://doi.org/10.1016/j.ijplas.2020.102779>.
- Sedighiani, K., Traka, K., Roters, F., Raabe, D., Sietsma, J., Diehl, M., 2021. Determination and analysis of the constitutive parameters of temperature-dependent dislocation-density-based crystal plasticity models. *Mechanics of Materials*. Submitted for publication.
- Segurado, J., Lebensohn, R.A., Llorca, J., Tomé, C.N., 2012. Multiscale modeling of plasticity based on embedding the viscoplastic self-consistent formulation in implicit finite elements. *International Journal of Plasticity* 28 (1). <https://doi.org/10.1016/j.ijplas.2011.07.002>.
- Shanthraj, P., Eisenlohr, P., Diehl, M., Roters, F., 2015. Numerically robust spectral methods for crystal plasticity simulations of heterogeneous materials. *International Journal of Plasticity* 66, 31–45. <https://doi.org/10.1016/j.ijplas.2014.02.006>.
- Shoemake, K., 1985. Animating rotation with quaternion curves. *Computer Graphics (ACM)* 19 (3). <https://doi.org/10.1145/325165.325242>.
- Tasan, C.C., Diehl, M., Yan, D., Zambaldi, C., Shanthraj, P., Roters, F., Raabe, D., 2014. Integrated experimental-simulation analysis of stress and strain partitioning in multiphase alloys. *Acta Materialia* 81, 386–400. <https://doi.org/10.1016/j.actamat.2014.07.071>.
- Tasan, C.C., Hoefnagels, J.P.M., Diehl, M., Yan, D., Roters, F., Raabe, D., 2014. Strain localization and damage in dual phase steels investigated by coupled in-situ deformation experiments and crystal plasticity simulations. *International Journal of Plasticity* 63, 198–210. <https://doi.org/10.1016/j.ijplas.2014.06.004>.
- Vidyasagar, A., Tutcuoglu, A., Kochmann, D., 2018. Deformation patterning in finite-strain crystal plasticity by spectral homogenization with application to magnesium. *Computer Methods in Applied Mechanics and Engineering* 335, 584–609. <https://doi.org/10.1016/j.cma.2018.03.003>.
- Wang, D., Diehl, M., Roters, F., Raabe, D., 2018. On the role of the collinear dislocation interaction in deformation patterning and laminate formation in single crystal plasticity. *Mechanics of Materials* 125. <https://doi.org/10.1016/j.mechmat.2018.06.007>.
- Zhang, C., Li, H., Eisenlohr, P., Liu, W., Boehlert, C.J., Crimp, M.A., Bieler, T.R., 2015. Effect of realistic 3D microstructure in crystal plasticity finite element analysis of polycrystalline Ti-5Al-2.5Sn. *International Journal of Plasticity* 69. <https://doi.org/10.1016/j.ijplas.2015.01.003>.
- Zhang, H., Liu, J., Sui, D., Cui, Z., Fu, M.W., 2018. Study of microstructural grain and geometric size effects on plastic heterogeneities at grain-level by using crystal plasticity modeling with high-fidelity representative microstructures. *International Journal of Plasticity* 100. <https://doi.org/10.1016/j.ijplas.2017.09.011>.
- Zhao, P., Song En Low, T., Wang, Y., Niezgoda, S., 2016. An integrated full-field model of concurrent plastic deformation and microstructure evolution: Application to 3D simulation of dynamic recrystallization in polycrystalline copper. *International Journal of Plasticity* 80. <https://doi.org/10.1016/j.ijplas.2015.12.010>.
- Zhao, Z., Kuchnicki, S., Radovitzky, R., Cuitiño, A., 2007. Influence of in-grain mesh resolution on the prediction of deformation textures in fcc polycrystals by crystal plasticity FEM. *Acta Materialia* 55 (7), 2361–2373. <https://doi.org/10.1016/j.actamat.2006.11.035>.